

1 **The GEWEX LandFlux project: evaluation of model evaporation using tower-**
2 **based and globally-gridded forcing data**

3

4 **Matthew F. McCabe^{1*}, Ali Ershadi¹, Carlos Jimenez², Diego G. Miralles³, Dominik Michel⁴**
5 **and Eric F. Wood⁵**

6 [1] {Division of Biological and Environmental Sciences and Engineering, King Abdullah University
7 of Science and Technology, Thuwal, Saudi Arabia}

8 [2] {Estellus, Paris, France}

9 [3] {Department of Earth Sciences, VU University Amsterdam, Amsterdam, The Netherlands}

10 [4] {Institute for Atmospheric and Climate Sciences, ETH Zurich, Zurich, Switzerland}

11 [5] {Department of Civil and Environmental Engineering, Princeton University, Princeton, United
12 States of America}

13 * Correspondence to: matthew.mccabe@kaust.edu.sa

14

15 **Abstract**

16 Determining the spatial distribution and temporal development of evaporation at regional and
17 global scales is required to improve our understanding of the coupled water and energy cycles
18 and to better monitor any changes in observed trends and variability of linked hydrological
19 processes. With recent international efforts guiding the development of long-term and globally
20 distributed flux estimates, continued product assessments are required to inform upon the
21 selection of suitable model structures and also to establish the appropriateness of these multi-
22 model simulations for global application. In support of the objectives of the GEWEX LandFlux
23 project, four commonly used evaporation models are evaluated against data from tower-based
24 eddy-covariance observations, distributed across a range of biomes and climate zones. The
25 selected schemes include the Surface Energy Balance System (SEBS) approach, the Priestley-
26 Taylor Jet Propulsion Laboratory (PT-JPL) model, the Penman-Monteith based Mu model (PM-

27 Mu) and the Global Land Evaporation Amsterdam Model (GLEAM). Here we seek to examine
28 the fidelity of global evaporation simulations by examining the multi-model response to varying
29 sources of forcing data. To do this, we perform parallel and collocated model simulations using
30 tower-based data together with a global-scale grid-based forcing product. Through quantifying
31 the multi-model response to high-quality tower data, a better understanding of the subsequent
32 model response to coarse-scale globally gridded data (that underlies the LandFlux product) can
33 be obtained, while also providing a relative evaluation and assessment of model performance.

34 Using surface flux observations from forty-five globally distributed eddy-covariance stations as
35 independent metrics of performance, the tower-based analysis indicated that PT-JPL provided
36 the highest overall statistical performance (0.72 ; 61 W.m^{-2} ; 0.65), followed closely by GLEAM
37 (0.68 ; 64 W.m^{-2} ; 0.62), with values in parenthesis representing the R^2 , $RMSD$ and Nash-Sutcliffe
38 Efficiency (NSE), respectively. PM-Mu (0.51 ; 78 W.m^{-2} ; 0.45) tended to underestimate fluxes,
39 while SEBS (0.72 ; 101 W.m^{-2} ; 0.24) overestimated values relative to observations. A focused
40 analysis across specific biome types and climate zones showed considerable variability in the
41 performance of all models, with no single model consistently able to outperform any other.
42 Results also indicated that the global gridded data tended to reduce the performance for all of
43 the studied models when compared to the tower data, likely a response to scale mismatch and
44 issues related to forcing quality. Rather than relying on any single model simulation, the spatial
45 and temporal variability at both the tower- and grid-scale highlighted the potential benefits of
46 developing an ensemble or blended evaporation product for global scale LandFlux applications.
47 Challenges related to the robust assessment of the LandFlux product are also discussed.

48

49 **1 Introduction**

50 Characterizing the exchange of water between the land surface and the atmosphere is a topic
51 of multi-disciplinary interest, as the processes that comprise this dynamic cycling of water
52 determine the spatial and temporal variability of hydrological responses across local and global
53 scales. In recent years, there has been significant progress in the development of regional and
54 global datasets based largely on remote sensing retrievals. These data have provided a wealth

55 of spatially and temporally varying information across a range of Earth system processes,
56 including soil moisture (Liu et al., 2011a), vegetation change (Tucker et al., 2005; Liu et al.,
57 2011b; Liu et al., 2013), groundwater (Famiglietti et al., 2011; Richey et al., 2015) and
58 precipitation (Huffman et al., 1995; Nesbitt et al., 2004), enabling a capacity to enhance our
59 understanding and description of regional- and global-scale water cycles and their spatial and
60 temporal variability. While evaporation represents the key process returning the Earth's surface
61 water to the overlying atmosphere and provides the linking mechanism between the water and
62 energy cycles, it is only in relatively recent times that effort has been directed towards the
63 development of global products (Mu et al., 2007; Fisher et al., 2008; Vinukollu et al., 2011a).

64 To address this observation limitation, a number of evaporation modelling approaches have
65 been developed over the past few years to enable estimation at scales beyond the field, using
66 satellite remote sensing (Sheffield et al., 2010; Miralles et al., 2011a) and other data sources
67 (Douville et al., 2013). The models tend to differ in their level of empiricism and in the desired
68 scale of application, with some exclusively developed for farm-scale operation and requiring
69 local calibration (Bastiaanssen et al., 1998; Allen et al., 2007). Others have been developed for
70 broader scale application and are built on physical relationships describing the water and
71 energy transfer at the land surface (Norman et al., 1995; Su, 2002; Fisher et al., 2008; Miralles
72 et al., 2011a). While traditional applications of evaporation estimates have been directed
73 towards agricultural monitoring (Allen, 2000), catchment water budgets and basin-scale water
74 management (Kustas et al., 1994; Granger, 2000), more recent applications of evaporation
75 products have included detection and prediction of heatwaves (Hirschi et al., 2011; Miralles et
76 al., 2014a), droughts (Mu et al., 2012; Otkin et al., 2014) and in resolving the likely contribution
77 of human-induced climate change on such events (Greve et al., 2014).

78 Despite the importance of understanding the magnitude and spatial and temporal variability of
79 evaporation, the availability of long-term products required to do this are rather limited.
80 Characterizing the long-term trends and variability in independent observations of the Earth's
81 coupled water and energy cycles is a key objective of the World Climate Research Programmes
82 (WCRP) Global Energy and Water Cycle Exchanges (GEWEX) project. Towards this task, the
83 GEWEX Data and Assessments Panels (GDAP) LandFlux project has coordinated two interrelated

84 research efforts that seek to: i) intercompare long-term gridded surface flux data sets and
85 identify their skill and reliability (i.e. product-benchmarking), and ii) simulate and intercompare
86 evaporation models to identify algorithms appropriate for developing a global flux product (i.e.
87 model-benchmarking). In one of the first global-scale product assessments, Jiménez et al.
88 (2011) examined twelve evaporation products obtained from satellite-based, reanalyses and
89 off-line LSM simulations for a 3 year period (1993-1995), identifying large correlations between
90 the products, similarity in their spatial distributions, as well as large absolute differences in the
91 annual average evaporation. A complementary investigation of the inter-product differences
92 was undertaken by Mueller et al. (2011), which included forty-one global evaporation data sets
93 across a range of satellite-based simulations, LSMs, Global Circulation Models (GCMs),
94 atmospheric reanalyses datasets, empirical up-scaling of eddy-covariance measurements, as
95 well as atmospheric water budget data sets. In that study, Mueller et al. (2011) used seven
96 years of monthly mean data for the period 1989-1995 and found strong similarity in the
97 absolute magnitude and spatial distribution of evaporation amongst the products. More
98 recently, Mueller et al. (2013) examined multi-annual trends and variations in evaporation
99 products from a range of diagnostic data sets, LSMs and reanalysis products and showed
100 consistency in inter-annual variations of evaporation products that corresponded well with
101 previous investigations (Jung et al., 2010).

102 These benchmarking studies provided a thorough (and much needed) assessment of available
103 global evaporation products and the varying approaches used to derive them. However,
104 evaluation of the models for their predictive skill was challenging due to inconsistencies in the
105 forcing data used to drive the models, as well as to the different parameterization schemes
106 employed. That is, the analysis was performed on the published evaporation output, rather
107 than re-running simulations from a common forcing dataset. In these benchmarking studies,
108 the evaporation data sets were also aggregated to similar spatial and temporal resolutions for a
109 common analysis period, to enable unbiased comparison. Uncertainties emerging from such
110 aggregations can often reduce the confidence in any such model performance ranking. One
111 initial effort addressing this was the study of Vinukollu et al. (2011a), which used the Surface
112 Energy Balance System (SEBS) model (SEBS; Su, 2002), a two-source Penman-Monteith scheme

113 by Mu et al. (2007) and a three-source model based on parameterizing the Priestley-Taylor
114 model (PT-JPL) (Fisher et al., 2008) to estimate global evaporation for the period 2003-2004.
115 The Vinukollu et al. (2011a) analysis revealed that the modelled instantaneous evaporation
116 (coinciding with the time of satellite overpass) was in reasonable agreement with locally-
117 observed evaporation at twelve eddy-covariance towers across the United States, with
118 correlations ranging from 0.43 to 0.54. However, uncertainties resulting from scale mismatch
119 between satellite data and the validation tower footprint reduced the confidence and skill
120 ranking of the models. One of the unique aspects of the present study is that tower data are
121 consistent across all model simulations: that is, tower-bias is minimized, by ensuring that all
122 models are assessed against the same tower records. Further, even though sub-grid scale
123 variability is not explored here (since none of the models explicitly account for this), the tower-
124 to-grid scale analysis acts as a diagnostic of representativeness and point-to-pixel error.

125 Recently, Ershadi et al. (2014) examined a number of models including SEBS, PT-JPL, the
126 Advection-Aridity model of Brutsaert and Stricker (1979) and a single-source Penman-Monteith
127 (PM) model (Monteith, 1965), using a set of twenty flux towers distributed across a range of
128 biome types and climate zones to force the models with tower-based data directly. Based on
129 common forcing and considering overall results, the study found that PT-JPL was the best
130 performing model, followed by SEBS, PM and Advection-Aridity. In a related contribution,
131 Ershadi et al. (2015) provided a more focused analysis on the influence of model structure and
132 resistance parameterization on single, two-layer and three-source Penman-Monteith models.
133 The authors identified considerable variability in the performance of models due to their
134 structure and parameterization choices.

135 A parallel effort to the LandFlux project is the European Space Agency (ESA) funded WAter
136 Cycle Multi-mission Observation Strategy for EvapoTranspiration (WACMOS-ET; see
137 <http://wacmoset.estellus.eu/>). WACMOS-ET, which is focused on an analysis period covering
138 2005-2007, seeks to better understand the impacts of model structure on flux estimation, with
139 an additional focus on developing a consistent forcing dataset using predominantly European
140 Space Agency developed products. A key result from these early works and the preliminary
141 outcomes from WACMOS-ET support the finding that no single model or parameterization

142 consistently outperformed any other across different biomes. Further details on these
143 complimentary efforts can be found in Michel et al. (2015) and Miralles et al. (2015).

144 While establishing a baseline level of performance at the tower scale is important,
145 understanding the impact of using the large-scale globally-gridded forcing that will ultimately
146 drive the global products is key. The focus of the current investigation is to build upon these
147 past efforts and complement ongoing WACMOS-ET investigations, by simulating state-of-the-
148 art evaporation models using a parallel assessment of tower-based meteorology and gridded
149 data, and comparing results with available eddy-covariance flux observations. Understanding
150 how application of gridded forcing data might influence the performance of the different
151 models, relative to their performance when forced with (presumably) higher-quality tower
152 data, is a motivating rationale for this work. Such evaluations are important in developing
153 insight into the sensitivity of the models to input data uncertainties, provide a relative
154 assessment of model quality and also inform upon issues of spatial scale and footprint
155 mismatch (McCabe and Wood, 2006). Establishing model suitability for large-scale operational
156 application as part of the GEWEX Landflux project is a further motivating goal for this work. As
157 such, a major objective is to evaluate the individual model responses across a range of biomes
158 and climate zones. The models selected for assessment include SEBS, PT-JPL, the Penman-
159 Monteith based Mu model (PM-Mu) (Mu et al., 2011) as well as the Global Land Evaporation
160 Amsterdam Methodology (GLEAM) (Miralles et al., 2011a). These models satisfy a number of
161 criteria that were considered important for global model selection, including reliance on a
162 minimum number of forcing variables, capacity to use remote sensing based observations, as
163 well as previous application at either the regional or global scale.

164

165 **2 Data and Methodology**

166 **2.1 Data**

167 For this analysis, model simulations cover the period from 1997 to 2007 and are performed at a
168 3-hourly temporal resolution. To examine model response and inter-product variability, a

169 parallel tower- and grid-based analysis was performed. Data for the tower-based analysis are
170 derived from a set of forty-five eddy-covariance towers (see Table A1), while the gridded data
171 are extracted from a compilation of available globally distributed satellite, meteorological and
172 land surface characteristics products. Compared to the 0.5 degree and 3-hourly gridded data,
173 the use of tower-based forcing is expected to minimize issues related to footprint uncertainties
174 when evaluating simulations against the observed eddy-covariance based flux data. The
175 primary purpose of the grid-based analysis is to better understand the effects of large-scale
176 forcing data on the accuracy of global retrievals, relative to the tower-based evaluations.

177 **2.1.1 Description of tower-based forcing data**

178 Data for the tower-based analyses are derived from forty-five eddy-covariance towers selected
179 from within the FLUXNET database (Baldocchi et al., 2001). Table A1 lists the key attributes of
180 the selected towers and Figure A1 describes the varying temporal lengths of the tower records
181 used in this study. The requirement that towers only be used if they are able to provide the
182 input data required by all models (see Table 1) was a strong limiting criterion that significantly
183 reduced the number of available study sites. In particular, the availability of land surface
184 temperature data, which is required for SEBS, drastically constrained the choice of towers.
185 However, ensuring data consistency within the towers used for simulation and assessment was
186 an important component of this work, as it removes the impact of tower bias in subsequent
187 model assessment. Even with this reduced number, the selected towers represent a
188 considerable spatial spread encompassing a variety of biome types and climate zones (see
189 Figure 1).

190 In terms of forcing data requirements, tower-based variables that were used for model
191 simulations include air temperature, relative humidity, wind speed, net radiation, ground heat
192 flux and precipitation. A summary of the forcing data requirements for each model is provided
193 in Table 1. Land surface emissivity, leaf area index and fractional vegetation cover were
194 estimated from Normalized Difference Vegetation Index (NDVI) data obtained from the Global
195 Inventory Monitoring and Modelling Study (GIMMS) dataset (Tucker et al., 2005), at 8 km
196 spatial and bi-monthly temporal resolutions. Here, the emissivity was calculated using the

197 approach of Sobrino et al. (2004), leaf area index was estimated following Fisher et al. (2008)
198 and the fractional vegetation cover was estimated using the technique described in Jiménez-
199 Muñoz et al. (2009). Land surface temperature was calculated using tower-observed longwave
200 upward radiation and by inverting the Stefan-Boltzmann equation (Brutsaert, 2005).
201 Atmospheric pressure data, which are absent from many towers, were calculated based on
202 ground elevation of tower locations using an equation presented in Bos et al. (2008). Canopy
203 height (h_c), which is needed for the SEBS model, was obtained from tower metadata and was
204 assumed constant during the simulation period. Although h_c varies over many vegetation types,
205 accounting for its within- and inter-annual variability is usually not possible, as observed data of
206 h_c variations are rarely recorded. Tower data were aggregated (i.e. summed for precipitation
207 and averaged for other input variables) from their native resolution of half-hourly or hourly to
208 3-hourly, to match the temporal resolution of the gridded data.

209 **2.1.2 Description of grid-based forcing data (LandFlux Version 0 forcing dataset)**

210 Grid-based data were developed by Princeton University for the LandFlux Version 0 (V-0)
211 dataset. The variables in the V-0 include air temperature, land surface temperature, wind
212 speed, atmospheric pressure, specific humidity, precipitation, net radiation, NDVI and leaf area
213 index. Net radiation data derive from the GEWEX Surface Radiation Budget (SRB) Version-3
214 (Stackhouse et al., 2011), while land surface temperature is determined by employing a
215 Bayesian post-processing procedure that merges High-Resolution Infrared Radiation Sounder
216 (HIRS) retrievals with the land surface temperature data from the National Centers for
217 Environment Prediction (NCEP) Climate Forecast System Reanalysis (CFSR) (Saha et al., 2010), as
218 described in Coccia et al. (2015). Precipitation data are also from the NCEP CFSR product and
219 have been bias-corrected to the Global Precipitation Climatology Project (GPCP) V2.2 dataset
220 (Adler et al., 2003). Likewise, atmospheric pressure, specific humidity and wind speed data
221 were extracted from the CFSR reanalysis data. For vegetation based parameters, NDVI data
222 were prepared by aggregating 8-km resolution GIMMS NDVI data to 0.5° resolution, while leaf
223 area index data were developed by Zhu et al. (2013) through fitting GIMMS NDVI data to the
224 Moderate Resolution Imaging Spectroradiometer (MODIS) MOD15A2 NDVI product, using a
225 neural network technique.

226 The majority of variables in the global LandFlux V-0 forcing dataset are at 0.5° spatial and 3-
227 hourly temporal resolution. Exceptions include the net radiation (1° and 3-hourly), NDVI (0.5°
228 and bi-monthly) and leaf area index (0.5° and monthly). For net radiation, the 1° data were
229 linearly interpolated to a 0.5° resolution. The bi-monthly NDVI data were assumed constant for
230 all 3-hourly time steps during each 15-day interval, while the leaf area index data were assumed
231 constant during each month. The canopy height over shrubland and forest biomes was
232 assumed fixed and was estimated using a static canopy height product developed by Simard et
233 al. (2011). For grassland and cropland biomes, where the dynamics of canopy height can be
234 considerable, canopy height was calculated using Equation 1, derived from Chen et al. (2012):

$$235 \quad h_c = h_c^{min} + \frac{h_c^{max} - h_c^{min}}{NDVI_{max} - NDVI_{min}} \times (NDVI - NDVI_{min}) \quad (1)$$

236 where h_c^{min} and h_c^{max} are the minimum and maximum canopy height and were obtained from
237 the static vegetation table of the North American Data Assimilation System (NLDAS) (available
238 from <http://ldas.gsfc.nasa.gov/nldas/web/web.veg.table.html>). $NDVI_{min}$ and $NDVI_{max}$ are the
239 minimum and maximum NDVI, respectively, and were calculated on a pixel-wise basis for each
240 calendar year. The JPL static vegetation height was aggregated linearly from 1 km to 0.5°.
241 Likewise, the NDVI derived canopy height was calculated at 8 km resolution and then
242 aggregated to 0.5°. Similar to the tower-based data, the methodology of Jiménez-Muñoz et al.
243 (2009) was used for the gridded forcing to estimate the fractional vegetation cover data from
244 NDVI data. The ground heat flux at the grid-scale was calculated as a fraction of net radiation
245 using fractional vegetation cover, following Su (2002).

246 **2.1.3 Model specific forcing data and data sources**

247 In addition to the data described above and shown in Table 1, both GLEAM and SEBS have some
248 model specific forcing data requirements. For SEBS, information on land surface temperature,
249 wind-speed and canopy height are required. At the tower-scale, these data are provided by
250 available meteorological forcing or meta-data descriptions in the case of canopy height. At the
251 grid-scale they are provided by a combination of the LandFlux V-O dataset and an adapted JPL
252 static vegetation height, as described in Section 2.1.2. GLEAM based simulations require

253 information on soil properties, vegetation optical depth (VOD), satellite soil moisture, snow
254 water equivalent, lightning frequency and vegetation cover fraction. Soil properties data for
255 GLEAM include field capacity, critical soil moisture and wilting point soil moisture thresholds.
256 Data for these were obtained from the Global Gridded Surfaces of Selected Soil Characteristics
257 dataset of the International Geosphere-Biosphere Programmes Data and Information System
258 (IGBP-DIS), available from Oak Ridge National Laboratory Distributed Active Archive Center
259 (<http://www.daac.ornl.gov>). Soil properties data were used in their native 5 arc-minute
260 resolution for tower-based analysis, but were aggregated to 0.5° for grid-based assessment.
261 Vegetation optical depth data was from Liu et al. (2011b) using a merged product from multiple
262 microwave based satellite data. The 0.25° spatial and daily temporal resolutions VOD data were
263 gap-filled as described by Miralles et al. (2011a). Soil moisture data assimilated in GLEAM
264 comes from the CCI-WACMOS dataset (Liu et al., 2012) produced from both active and passive
265 satellite microwave data at 0.25° and daily resolution. Snow water equivalent data are from the
266 GlobSnow product version 1.0 (Luo et al., 2010); as GlobSnow covers the northern
267 hemisphere only, Global Monthly Snow Water Equivalent Climatology data from the National
268 Snow and Ice Data Center (NSIDC) (Armstrong et al., 2005) are used for the BW-Ma1 tower (see
269 Table A1) located in the southern hemisphere. Both GlobSnow data and the NSIDC product are
270 at approximately 0.25° spatial and daily temporal resolutions. Lightning frequency data is based
271 on the Combined Global Lightning Flash Rate Density monthly climatology at 0.5° (Mach et al.,
272 2007) and it is used to calculate a climatology of rainfall rates (Miralles et al., 2010). Finally,
273 vegetation cover fractions are derived from the MODIS MOD44B product (Hansen et al., 2005).
274 The MODIS continuous cover fractions describe every pixel as a combination of its fractions of
275 water, tall canopy, short vegetation and bare soil. The temporal average of fractions is used
276 here for the MODIS period, providing only a static cover fraction for the GLEAM simulations.
277 The MOD44B product is available at 250 m and 0.25° resolution. For tower-based analysis,
278 cover fractions are at 250 m resolution, but for grid-based analysis the 0.25° MOD44B product
279 was aggregated to 0.5°.

280 Table 1 summarizes the different sources and spatio-temporal scales of the data that were used
281 for both the tower- and grid-based flux simulations. As noted earlier, the temporal analysis

282 encompasses the period 1997-2007, although as defined in Figure A1, the individual tower
283 records do not necessarily provide uninterrupted observations during this time range.

284 **2.1.4 Definition of selected biome type and climate zones**

285 The specific biomes examined in this work include wetland (WET), grassland (GRA), cropland
286 (CRO), shrubland (SHR), evergreen needleleaf forest (ENF), evergreen broadleaf forest (EBF) and
287 deciduous broadleaf forest (DBF). Biome type was specified in Fluxnet metadata records for
288 each of the individual tower sites and follows the International Geosphere-Biosphere
289 Programme (IGBP) classification. For simplicity, the shrubland biome is comprised of closed
290 shrubland, woody savannah and mixed forest biomes. The number of towers for each biome
291 type varies, with fourteen for evergreen needleleaf forest, ten for grassland, seven for
292 cropland, seven for deciduous broadleaf forest, four for shrubland, two for wetland and only
293 one for evergreen broadleaf forest (see Table A1). The climate zones include boreal (BOR), sub-
294 tropical (subTRO), temperate (TEMP), temperate-continental (TempCONT) and dry (DRY) for
295 arid and semi arid regions. These zones were prescribed from the tower specific metadata,
296 which were in turn derived from Rubel and Kottek (2010), based on a Köppen-Geiger climate
297 classification. As with biome type, the towers are not evenly distributed across climate zones,
298 with fifteen for temperate, eleven for sub-tropical, eight for temperate-continental, five for
299 boreal and six for dry regions (see Table A1).

300 **2.2 LandFlux Model Descriptions**

301 Following are brief descriptions of the models employed in this analysis. For a more
302 comprehensive explanation of the implementation of these different schemes, the reader is
303 referred to the principal model references as well as the recent contributions of Ershadi et al.
304 (2014) and Ershadi et al. (2015).

305 **2.2.1 SEBS**

306 SEBS is a widely employed process-based model used in the estimation of evaporation. The
307 model uses a variety of land surface and atmospheric variables and parameters for simulating
308 the transfer of heat and water vapor from the land surface to the atmosphere. To do so, the

309 model first estimates the representative roughness of the land surface and then uses roughness
310 parameters, temperature gradient and wind speed data to estimate sensible heat flux via a set
311 of flux-gradient equations describing the transfer of heat from the land surface to the
312 atmosphere. Depending on the atmospheric boundary layer height, the model uses either the
313 Monin-Obukhov Similarity Theory or the Bulk Atmospheric Similarity Theory equations
314 (Brutsaert, 2005). The model estimates the sensible heat flux of hypothetically wet and dry
315 conditions and uses these extreme-cases to calculate the evaporative fraction. Evaporation is
316 then calculated as a fraction of the available energy. The model requires accurate values of net
317 radiation, land surface temperature, air temperature, humidity, wind speed and vegetation
318 phenology to calculate surface fluxes. SEBS relaxes the need for parameterization of the surface
319 resistance, but is sensitive to aerodynamic resistance parameterization (Ershadi et al., 2013).
320 Further details on SEBS and its model formulation can be found in Su (2002).

321 **2.2.2 PT-JPL**

322 The PT-JPL model of evaporation uses a minimum of meteorological and remote sensing data
323 and has been employed in a number of studies to estimate regional and global scales flux
324 response (Fisher et al., 2008; Sahoo et al., 2011; Vinukollu et al., 2011b; Vinukollu et al., 2011a;
325 Badgley et al., 2015). A key characteristic of the model is the use of bio-physiological properties
326 of the land surface to reduce Priestley-Taylor potential evaporation to actual values. The PT-JPL
327 is a three source model in which the total evaporation is partitioned into soil evaporation (λE_s),
328 canopy transpiration (λE_t), and wet canopy evaporation (λE_i), i.e. $\lambda E = \lambda E_s + \lambda E_t + \lambda E_i$. The
329 model first partitions the total net radiation to soil and vegetation components and calculates
330 potential evaporation for soil, for canopy and for the wet canopy. The model then determines a
331 set of constraint multipliers to represent the impacts of green canopy fraction, relative wetness
332 of the canopy, air temperature, plant water stress and soil water stress on the evaporative
333 process. The model uses the constraint multipliers to reduce the potential evaporation to actual
334 values for each component of the system. PT-JPL does not calibrate or tune parameter values
335 and does not use wind speed data or parameterizations of the aerodynamic and surface
336 resistances. However, the model does require accurate estimates of optimum temperature

337 (T_{opt}) (Potter et al., 1993) for canopy transpiration. The optimum temperature is the air
338 temperature at the time of peak canopy activity, when the highest values of absorbed
339 photosynthetically active radiation and minimum values of vapour pressure deficit occur.
340 Further details of the PT-JPL model can be found in Fisher et al. (2008).

341 **2.2.3 PM-Mu**

342 The PM-Mu was expanded from a two-source Penman-Monteith implementation (Mu et al.,
343 2007) to a three-source version (Mu et al., 2011), which forms the basis behind the near real-
344 time estimation of global evaporation in the MOD16 product (Mu et al., 2013) (n.b. the PM-Mu
345 nomenclature used herein reflects an identical description used in Michel et al. (2015) and
346 Miralles et al. (2015), where it is referred to as PM-MOD). Evaporation in the PM-Mu model is
347 the sum of soil evaporation, canopy transpiration and evaporation of the intercepted water in
348 the canopy, i.e. ($\lambda E = \lambda E_s + \lambda E_t + \lambda E_i$). Estimation of evaporation for interception and
349 transpiration components is based on the Penman-Monteith equation (Monteith, 1965). Actual
350 soil evaporation is calculated using potential soil evaporation and a soil moisture constraint
351 function from the Fisher et al. (2008) ET model. This function is based on the complementary
352 hypothesis (Bouchet, 1963), which defines land-atmosphere interactions from air vapour
353 pressure deficit and relative humidity. Evaporation components are weighted based on the
354 fractional vegetation cover, relative surface wetness and available energy. Parameterization of
355 aerodynamic and surface resistances for each source is based on extending biome specific
356 conductance parameters from the stomata to the canopy scale, using vegetation phenology
357 and meteorological data. In contrast to the majority of Penman-Monteith type of models, the
358 PM-Mu does not require wind speed and soil moisture data for parameterization of resistances.
359 However, global application of the model requires consideration of the fact that resistance
360 parameters were calibrated against data from a set of eddy-covariance towers. One
361 consideration that may influence model simulations is that this parameterization approach was
362 developed at the daily-scale. However, both the present and also a recent related study
363 (Miralles et al. 2015) suggest no obvious impact for sub-daily application. Further details on
364 PM-Mu can be found in Mu et al. (2011) and Mu et al. (2013).

365 **2.2.4 GLEAM**

366 GLEAM (Miralles et al., 2011a) has been used not only in estimating global evaporation
367 (Miralles et al., 2011b) but also in detection and evaluation of heatwaves (Miralles et al.,
368 2014a), climate variability (Miralles et al., 2014b) and land-atmospheric feedbacks (Guilod et
369 al., 2015). Designed as a satellite data based model, GLEAM first estimates interception loss
370 using the analytical method of Gash (1979) and then applies the Priestley-Taylor equation to
371 calculate potential evaporation for soil and vegetation. Like PT-JPL, the model constrains the
372 potential evaporation values to actual values by applying a stress factor, although GLEAM is
373 based on different assumptions and encompasses both moisture availability in a multi-layered
374 soil system and vegetation water content inferred from vegetation optical depth data (Liu et al.,
375 2011b). In contrast to SEBS, PT-JPL and PM-Mu, the GLEAM model is equipped with routines to
376 quantify sublimation of snow-covered regions, to estimate open-water evaporation and to
377 assimilate remote sensing soil moisture data. Routine application of GLEAM is usually
378 performed in time-series mode, in which the model tracks the changes of soil moisture state
379 across time steps. Here, to allow application of the model at the tower-scale, gaps in the tower
380 data were filled by establishing correlation between the variables in tower- and grid-based
381 data. Simulated evaporation values were filtered from the analysis for these gap-filled periods.
382 Further details on GLEAM can be found in Miralles et al. (2011a;b).

383 **2.3 Model Simulation and Analysis**

384 The four selected models were forced with both tower- and grid-based data. The results were
385 then filtered for daytime-only periods, defined as when the shortwave downward radiation
386 exceeds 20 W.m^{-2} , to avoid issues associated with negative net radiation and night-time
387 condensation. The data were also filtered for rain events, for negative sensible and latent heat
388 flux observations, for low quality or gap-filled tower records, for frozen land surfaces and for
389 times in which air temperature was less than or equal to $0 \text{ }^{\circ}\text{C}$. The performance of the models
390 was evaluated for individual towers, for the collection of data from all towers, for towers
391 classified across biome types and for towers classified across climate zones.

392 To evaluate the skill of the models, we used traditional scatterplots and common statistical
393 metrics including the coefficient of determination (R^2), slope (m) and y-intercept (b) of the
394 linear regression, the root-mean-square difference ($RMSD$), relative error [$RE =$
395 $RMSD/\text{mean}(\lambda E_{obs})$] and the Nash-Sutcliffe Efficiency (NSE) (Nash and Sutcliffe, 1970). In
396 developing these performance metrics, simulated evaporation was compared with tower-
397 observed evaporation (λE_{obs}) that were corrected for non-closure using the energy residual
398 technique, as described in Ershadi et al. (2014). Scatterplots of matching percentiles (referred
399 to hereafter as percentile plots) of observed evaporation versus simulated values from the 1st
400 to 99th percentile increment were also used (Section 3.1). The 25th percentile (Q_{25}), median
401 (Q_{50}) and 75th percentile (Q_{75}) were used for further model assessment. To establish the
402 response of the models to water availability at individual tower sites, we calculated an aridity
403 index as $AI = P/E_p$, with P the annual precipitation (mm.yr^{-1}) and E_p the annual potential
404 evaporation (mm.yr^{-1}), calculated using a Priestley-Taylor equation and assuming an alpha-
405 coefficient of 1.26. LandFlux V-0 data (Section 2.1.2) at 3-hourly resolution were used to
406 calculate aridity index values and an average value was calculated to represent the state of
407 water availability at specific tower locations.

408

409 **3 Results**

410 **3.1 Relative performance of the models when using tower-based and gridded data**

411 Figure 2 and Figure 3 show scatterplots, percentile plots and relevant statistical metrics of the
412 modelled evaporation for all of the available 3-hourly data records from across the forty-five
413 towers (representing 115,148 records in total). For the tower-based analysis (see Figure 2), PT-
414 JPL presents the best overall performance with lower model spread and an $RMSD = 61 \text{ W.m}^{-2}$,
415 $RE = 0.41$, $R^2 = 0.71$ and an $NSE = 0.65$. The model slightly underestimates evaporation, with a
416 slope of linear regression equal to 0.91 and with the majority of the percentile plot (up to Q_{75})
417 located just under the 1:1 line. When considering results across all towers, GLEAM presents
418 comparable statistical performance to PT-JPL, with an $RMSD = 64 \text{ W.m}^{-2}$, $RE = 0.43$ and an $NSE =$
419 0.62 . GLEAM tends to slightly underestimate evaporation, with the slope of linear regression

420 equal to 0.84 and with the percentile plot being located under the 1:1 line. SEBS generally
421 overestimates evaporation and has the lowest overall performance, with an $RMSD = 101 \text{ W.m}^{-2}$,
422 $RE = 0.68$ and $NSE = 0.24$, even though it has one of the highest R^2 values at 0.72. For PM-Mu,
423 the model tends to underestimate evaporation, resulting in an $RMSD = 78 \text{ W.m}^{-2}$, $RE = 0.52$
424 and an $NSE = 0.45$. Overall, the PT-JPL and GLEAM seem to present as more robust candidate
425 models for estimation of evaporation, at least in terms of their statistical response at the tower
426 scale. All models show a large spread around the fitted linear regression line. While the
427 summary statistics are useful metrics of performance, the inter-tower variability of the models
428 is an important element of this work and will be discussed further in the following sections.

429 The effect of using globally-gridded forcing data on the evaporation models is presented in
430 Figure 3. Apart from providing a direct evaluation on the accuracy of the global LandFlux
431 product, assessing flux response to a change in forcing aids in diagnosing the model sensitivity
432 to data uncertainties (which are inherent in any data product). Likewise, an indirect assessment
433 of the issue of footprint mismatch between the gridded data (0.5°) and the eddy-covariance
434 tower (hundreds of meters) can also be inferred. Figure 3 clearly shows that use of the grid-
435 based data reduces the performance of all models relative to the tower-based runs, with all
436 statistics degrading with a change in forcing resolution. SEBS displayed the largest sensitivity to
437 forcing data, with a 0.4 decrease in NSE and a 28 W.m^{-2} increase in $RMSD$. The sensitivity of PT-
438 JPL and GLEAM to the use of gridded data was lower, with both showing an approximately 0.3
439 decrease in NSE and around 22 W.m^{-2} increase in $RMSD$ when assessing the grid-based analysis.
440 Overall, PM-Mu shows the lowest sensitivity to forcing, with a 0.26 decrease in NSE and 18
441 W.m^{-2} increase in $RMSD$, albeit presenting the lowest correlation and slope of linear regression
442 for all model responses.

443 Overall, these results confirm that all models display a relatively high sensitivity to changes in
444 the type and quality of input forcing data. While gridded forcing data are expected to have a
445 mismatch with the tower-based forcing due to their larger pixel (and footprint) sizes, this
446 spatial mismatch will impact all of the applied models, albeit to a lesser or greater extent,
447 depending on forcing data requirements. While spatial scale no doubt plays a major role in
448 decreasing model efficiencies at grid-scales, a key reason for the differences in tower- versus

449 grid-based results relates to internal inconsistencies within the gridded forcing data. For
450 instance, SEBS is known to be particularly sensitive to the temperature gradient between the
451 land surface and the atmosphere (van der Kwast et al., 2009; Ershadi et al., 2013). While the
452 temperature gradient at the tower scale is more reliable due to application of the tower-based
453 sensors for air temperature and land surface temperature, obtaining such consistency is harder
454 when different sources of forcing data are employed (see Section 2.1). Not surprisingly, results
455 also indicate that those models that use fewer inputs show lower sensitivity to changes in the
456 forcing. As such, any inconsistency between the tower and gridded data is likely to have less
457 influence on the PT-JPL, GLEAM and PM-Mu models than it will on SEBS, which in addition to
458 vegetation height, requires both land surface temperature and wind speed data: two variables
459 with considerable spatial variability. Disentangling the varying influence of model structural and
460 forcing data uncertainty requires focused attention and is examined further in the Discussion
461 section.

462 The large spread of data in the scatterplots indicates that there is considerable variability in the
463 performance of the models at individual towers, irrespective of whether tower or gridded data
464 are used. Of course, it may also be indicative of systematic biases in the in-situ data, which vary
465 from one tower to another and subsequently impact on model spread: however, this is non-
466 trivial to determine. To investigate the nature of this variability, we extend the analysis by
467 developing time series of R^2 , RE and NSE at 3-hourly resolution for individual tower locations, as
468 shown in Figure 4. To examine performance as a function of hydrological condition, the towers
469 are arranged by degree of increasing aridity, as determined by calculation of an aridity index
470 (see Section 2.3), with left-to-right representing the transition from wet-to-dry and describing
471 an aridity index varying between approximately 2 and 0.

472 From Figure 4 it can be observed that there is a general downward trend in both R^2 and NSE as
473 aridity increases, with a slight upward trend reflected in RE . In terms of R^2 , most of the models
474 (except for PM-Mu) show some consistency in performance until an aridity index of around 0.7,
475 wherein models start to diverge. Similar agreement is seen in the relative error plot, although
476 the outlier here is SEBS, which shows variable performance unrelated to aridity changes.
477 Examining the Nash-Sutcliffe efficiency allows for a clearer evaluation of model response to be

478 obtained. For this metric, PT-JPL and GLEAM display relatively good correspondence for most of
479 the towers, but start to diverge more regularly for aridity indices below 0.8. Overall, PT-JPL
480 presents a marginally better response than GLEAM, with higher values of NSE and R^2 and lowest
481 values of RE produced across the majority of towers. Similar results are expressed in Figure A2,
482 which presents the same tower based inter-comparison as in Figure 4, but for the grid-scale
483 model simulations.

484 From Figure 2 it was observed that SEBS presented the lowest values of NSE and highest values
485 of RE , while PM-Mu had the lowest values of R^2 . Highlighting the importance of examining a
486 range of statistical metrics, the R^2 values for SEBS are actually comparable to those of PT-JPL
487 and GLEAM, or even higher for a majority of towers that have an aridity index less than 0.7.
488 Inspection of individual tower-based scatterplots for each of the models (not shown) illustrated
489 that while the SEBS evaporation has a strong linear relationship with observed values for a
490 majority of towers, the linear regression line exhibits a large slope, indicating an overestimation
491 in SEBS predictions. Those towers that exhibit drops in NSE (and rise in RE) for the SEBS model
492 (e.g. DE-Tha, NL-Loo, US-Wrc, FR-Pue; see Table A1) are located mainly in shrubland and forest
493 biomes, suggesting a dependency of SEBS model performance that is tied to land surface
494 vegetation characteristics. Although statistical variations are evident in all models, the greater
495 response variability in SEBS is likely due to problems in simulating heat transfer within the
496 roughness sub-layer (RSL), which often forms over tall and heterogenous land surfaces
497 (Harman, 2012). We explore the issue of skill dependency of certain models to biome type and
498 climate zone in Sections 3.2 and 3.3.

499 As noted, Figure 4 shows a general decrease in the predictive skill in all models where towers
500 have an aridity index less than 0.7, but particularly so for PM-Mu and SEBS. These reductions
501 may in part be due to data uncertainties in tower observations that originate from the
502 advection of dry air into the tower footprint, or to a reduced capacity of the models to
503 reproduce the evaporative response when evaporation represents a small fraction of the total
504 available energy. Two towers at which all models display poor performance are IT-Noe and IL-
505 Yat (see Figure 1). It seems likely that IT-Noe is influenced by strong advection of moist air from
506 the Mediterranean Sea, while IL-Yat is influenced by advection of hot and dry air from

507 surrounding desert regions. None of the models in this study are able to specifically account for
508 advection and are thus prone to misrepresenting the observed evaporative response.

509 **3.2 Performance of the models across biomes**

510 The variability in model performance across the tower sites observed in Figure 4 and Figure A2,
511 indicates that a biome-specific assessment could be useful to determine whether the
512 performance of the models is also correlated to the underlying land cover, in addition to any
513 aridity influence. Figure 5 presents the R^2 , RE and NSE for each of the models for the seven
514 different biome classes. The analysis was conducted using the higher quality tower-based
515 simulations for all available 3-hourly data. One immediate highlight from Figure 5 is the
516 relatively poor performance of all models over shrubland sites, where low values of NSE (i.e.
517 $NSE \leq 0.05$) and reduced R^2 can be observed. Ershadi et al. (2014) observed a similarly poor
518 response over shrublands in a separate tower-based analysis that employed some of the same
519 models examined here. They attributed the result to difficulties in the parameterization of the
520 models over such landscapes due to the strong heterogeneities present in these environments,
521 as well as inherent water limitations. For instance, the capacity of the GIMMS NDVI data with 8
522 km spatial resolution is clearly insufficient in effectively parameterizing the roughness for SEBS,
523 resistances for PM-Mu and constraint functions for the PT-JPL.

524 Excluding shrublands from the analysis, the PT-JPL is one of the best performing models across
525 the remaining biomes, having the highest values of NSE and R^2 and lowest relative errors.
526 Consistency in the performance of PT-JPL across biome types has been reported in earlier
527 studies (Vinukollu et al., 2011a; Ershadi et al., 2014) and was variously ascribed to the
528 formulation of its constraint functions (see Section 2.2.2) and the minimal forcing data
529 requirements, which reduce its sensitivity to uncertainties in input data. GLEAM closely follows
530 PT-JPL for evergreen needleleaf forest and grassland biomes, but shows marginally lower NSE
531 values for other biomes. Figure 5 also indicates that while SEBS has relatively high values of R^2
532 over the majority of biome types, it fails to provide sufficient predictive skill for the estimation
533 of evaporation over shrublands and forest biomes. These biome types are characterized by tall
534 and heterogeneous canopies, within which the roughness sub-layer forms. The reduced

535 capacity of the SEBS flux gradient functions in simulating heat transfer within the roughness
536 sub-layer has been highlighted previously (Weligepolage et al., 2012; Ershadi et al., 2014).
537 Although performing poorly in shrubland and forest biomes, the SEBS model exhibits a
538 comparatively good performance across wetlands, grasslands and croplands, where shorter
539 canopies dominate. PM-Mu presents the lowest values of R^2 across all biomes, although the
540 model presents reasonable NSE values over cropland (0.64) and broadleaf forest (>0.54)
541 biomes. Improved performance of the PM-Mu model over croplands has been observed in a
542 recent study (Ershadi et al., 2015), but the key reasons for low R^2 values of the model across
543 other biomes is not immediately apparent and requires further investigation.

544 Percentile plots of the 3-hourly tower-based results were used to identify whether a model
545 under- or over-estimates evaporation across its distribution function. From Figure 6 it can be
546 seen that SEBS clearly overestimates while PM-Mu underestimates evaporation across all
547 biome types, reflecting those results presented in Figure 2. The percentile plots for SEBS are
548 close to the 1:1 line for grassland and cropland biomes that have short canopy height,
549 confirming the observations made for Figure 4 and Figure 5. PT-JPL shows good model
550 reproduction of observed values over grassland and deciduous broadleaf forest biomes, with
551 the percentile plots close to the 1:1 line. However, the model slightly underestimated
552 evaporation for croplands and overestimated evaporation for wetlands, with the tails
553 (percentiles greater than Q_{75}) reflecting greater divergence than the bulk of the distribution.
554 The rate of overestimation was higher for evergreen needleleaf forest, evergreen broadleaf
555 forest and for shrubland biomes. Figure 6 also shows that GLEAM presents strong performance
556 over grasslands, croplands and evergreen needleleaf forest sites, underestimated evaporation
557 across deciduous broadleaf forest sites and tended to overestimate evaporation across the
558 remaining biomes (wetlands, shrublands and evergreen broadleaf forests).

559 Overall, all models show a tendency towards reduced performance when applied over forest
560 biomes, but improved performance over shorter canopies. These results may be reflecting the
561 fundamental physical basis behind approaches such as the base Penman-Monteith (Penman,
562 1948), Priestley-Taylor (Priestley and Taylor, 1972) and Monin-Obukhov flux gradient functions,

563 which were developed for such surface types (Brutsaert, 1982), highlighting the challenges
564 inherent in global scale application of such models, especially over diverse land cover types.

565 To further evaluate the influence of biome type on evaporation estimation and to discriminate
566 the role of individual forcing variables in impacting model efficiencies, the *NSE* and R^2 values
567 between tower- and grid-based data were calculated for the flux response, as well as for key
568 forcing variables such as net radiation, land surface temperature, air temperature, wind speed,
569 specific humidity, fractional vegetation cover and leaf area index. As can be seen in Figure 7,
570 agreement between tower-based and grid-based net radiation data is relatively high across all
571 biomes, but especially so over forest biomes ($NSE \geq 0.67$). Grid-based wind speed data have the
572 most variable agreement with tower data, with R^2 and *NSE* values generally lower than other
573 selected variables across all of the examined biomes. Air temperature shows good agreement,
574 with both high *NSE* values ($NSE \geq 0.7$) and high R^2 values ($R^2 \geq 0.84$). Specific humidity data are
575 also well reproduced ($NSE \geq 0.72$), as is land surface temperature with an $NSE \geq 0.80$ for all
576 biomes. In sharing a common GIMMS-NDVI based derivation, the agreement for fractional
577 vegetation cover and leaf area index data is reasonable over the majority of biomes, except
578 over evergreen broadleaf forest, where both the R^2 and *NSE* are low.

579 The lower panel of Figure 7 show R^2 and *NSE* values for both the tower- and grid-based
580 simulations against eddy-covariance observations for each of the models, discriminated by
581 biome type. As can be seen, the performance of all models is reduced across all biomes when
582 grid-based forcing data is used, a result reflected in all cases by relatively lower *NSE* and R^2
583 values. PM-Mu had the smallest and SEBS had the largest decrease in performance over a
584 majority of the biomes, in accordance with the findings of Section 3.1. PT-JPL and PM-Mu had a
585 relatively constant decrease in *NSE* and R^2 for the grid-based simulations. Decreased modelling
586 performance was also maintained for GLEAM, except over the single evergreen broadleaf forest
587 tower, where a more significant departure (relative to the other biome types), was observed.
588 SEBS showed a much larger variability in performance reduction, with smaller variations due to
589 forcing over forest biomes and larger reductions over biomes with shorter canopies. The
590 significant decrease in *NSE* for SEBS over grassland, cropland and to some extent the wetland
591 biome, cannot be immediately associated with *NSE* or R^2 changes in any of the forcing variables.

592 It is interesting that the agreement over grassland and cropland biomes between tower- and
593 grid-based variables is amongst the highest (especially for wind speed, fractional vegetation
594 cover and for leaf area index data), yet the subsequent model performance is among the worst.
595 The use of global statistics to evaluate model response makes discriminating the cause of this
596 variability difficult. It is possible that the statistics are biased low due to the influence of one or
597 a few individual towers, by errors in the forcing fields driving model parameterizations (i.e.
598 vegetation height) or in response to model sensitivities to particular forcing variables. Either
599 way, these results highlight the difficulties in diagnosing the cause of performance response
600 and related sensitivity to forcing data variables in complex process-based models, which often
601 display a high degree of interactions between the variables. Indeed, diagnosing the forcing
602 variables responsible for reducing the efficiency of particular models is not feasible with a
603 simple correlation analysis of the input data fields, but requires a separate and focused
604 sensitivity analysis.

605 **3.3 Performance of the Models over Climate Zones**

606 Similar to the biome-wise analyses, an evaluation of the models was conducted across a
607 number of distinct climate zones, with R^2 , RE and NSE values for tower-based 3-hourly
608 evaporation estimations shown in Figure 8. Yet again, the results highlight the importance of
609 considering a range of evaluation metrics, as the models display some variability relative to the
610 statistical measure being employed. Overall, both PT-JPL and GLEAM maintain a consistently
611 good performance over the majority of climate zones, with PT-JPL expressing a slightly
612 improved response over all zones except temperate, where GLEAM shows an improved
613 simulation. In terms of R^2 , PM-Mu presents the lowest values overall, while SEBS exhibits high
614 values over the majority of climate zones, similar to the biome based analysis. However, SEBS
615 generally fails to reproduce the observed evaporation response, with high RE and low NSE . All
616 models have their best performance over the temperate-continental climate zone, with high
617 NSE and R^2 and low RE , which was followed closely by the temperate climate zone. The lowest
618 overall performance for all models corresponded to the dry climate zone, again reflecting the
619 aridity based results in Figure 4. As discussed in Section 3.1, data uncertainties due to the role

620 of advection in dry regions and difficulties in the accurate estimation when confronted with low
621 evaporative fractions are likely reasons behind such performance reductions in dry regions.

622 Figure 9 displays the corresponding percentile plots of model performance over the five
623 different climate zones. As can be seen, PT-JPL and GLEAM provide generally good performance
624 over all climate zones, although GLEAM slightly underestimates evaporation for temperate-
625 continental and boreal climate zones. SEBS overestimates relative to tower-based evaporation
626 across all biomes, while PM-Mu generally underestimates, except over temperate and
627 temperate-continental climate zones, for which the percentile plot of PM-Mu are relatively
628 close to the 1:1 line.

629 Similar to Figure 7, Figure 10 outlines the model response differentiated for the different
630 climate zones when using grid-based forcing data. As can be seen from the lower panel, the
631 simulation performance is reduced across all climate zones, relative to the tower data. In
632 particular, SEBS is significantly impacted across the majority of climate zones, with both a
633 reduction in NSE and R^2 , except over boreal forests. One possible reason for this smaller
634 variation over boreal forests could be due to lower surface-to-air temperature gradients over
635 forests, which contributes to smaller sensible heat fluxes and consequently larger evaporative
636 fraction values (in contrast to model performance over dry climates, where the temperature
637 gradient is large). Nevertheless, the relationship between uncertainty in individual variables and
638 the reduction of modelling performances is not able to be determined here. Further analysis
639 examining the sensitivity of individual models to their forcing is required.

640

641 **4 Discussion**

642 Understanding the role of model forcing in influencing simulation results, as well as examining
643 the impacts of biome type and climate zone on flux response, are important elements in the
644 development of robust globally-distributed evaporation products. The focus of this study was
645 on evaluating a set of process-based models, to support the development of globally
646 distributed and long term observations of surface fluxes as part of the GEWEX LandFlux project.
647 Overall, the PT-JPL and GLEAM models provided the most consistent performance, while PM-

648 Mu tended to underestimate and SEBS overestimate evaporation relative to the forty-five eddy-
649 covariance tower observations examined here. However, while statistical analysis allows a
650 pseudo-ranking of model performance, more detailed evaluation across towers, and biome and
651 climate types highlighted the considerable within-model variability in performance. Results also
652 demonstrated that changing the scale of input forcing data from tower- to grid-based reduced
653 the quality of model estimates in all cases, but especially for SEBS, where a sensitivity to
654 surface-air temperature gradients plays a strong role. In the following, we examine these
655 results and interpret any implications for large-scale global applications.

656 With its relatively simple modelling structure, PT-JPL performed consistently well relative to the
657 other models that have more complex structures and parameterization configurations. One
658 possible reason for this response may relate to the constraint functions of PT-JPL serving a wide
659 range of hydro-meteorological conditions, encompassing energy-limited (e.g. boreal climate) to
660 water-limited (e.g. dry climate) conditions. The good performance of PT-JPL was also observed
661 in a recent multi-model evaluation study, with a summary of the strengths and limitations of
662 the model presented in Ershadi et al. (2014). GLEAM also performed well, both at the tower
663 and at the grid-scale (see Figure 4 and Figure A2). Previous studies have shown that the model
664 is sensitive to the accuracy of precipitation data (Miralles et al., 2011b), as this determines the
665 partitioning of intercepted evaporation in the model and the root-zone soil moisture.
666 Unfortunately, testing for such sensitivities was not possible here, as both tower- and grid-
667 based records were filtered for rainfall events in post-processing steps, in response to the
668 limitation of eddy-covariance observations during such events.

669 In terms of the NSE , R^2 and RE , PM-Mu followed PT-JPL and GLEAM, with the model tending to
670 underestimate evaporation when applied to most of the tower- and grid-based records. While
671 reasons for this underestimation are not immediately clear, a recent study examining the
672 structure and parameterization of Penman-Monteith type models (Ershadi et al., 2015) showed
673 that the PM-Mu, which has a three-source structure, underperformed relative to a single-
674 source (Monteith, 1965) and a two-layer approach (Shuttleworth and Wallace, 1985) across all
675 studied biome types except croplands. An interesting aspect of Ershadi et al. (2015) was that
676 application of the canopy transpiration resistance scheme of the PM-Mu in those simpler

677 models improved their prediction skills. As such, the reduced performance of the PM-Mu
678 predictions might relate to underlying structural and parameterization issues in the model. As
679 the operational model behind the generation of the current MOD16 global evaporation product
680 (Mu et al., 2013), further studies to diagnose the cause of these responses are required.

681 Regarding assessment against the tower-based eddy-covariance observations, SEBS performed
682 relatively poorly in most statistical metrics when compared to the other models, as it
683 overestimated evaporation across a majority of studied biomes and climate zones, except over
684 grasslands and cropland sites with short canopies (e.g. less than 3 m). Interestingly, even
685 though generally over-predicting results, it had one of the highest R^2 values, indicating good
686 correlation with the eddy-covariance observations. Findings from Ershadi et al. (2014) confirm
687 the good performance of the model over short canopies and its lack of performance over
688 shrublands and forests. In terms of performance against underlying biome type, it was
689 observed that any performance reduction was observed mainly across shrublands and forest
690 biomes, where the roughness sub-layer forms above the canopy (Harman, 2012). Importantly,
691 the flux-gradient functions of the SEBS model are not parameterized to effectively simulate the
692 heat transfer process in the roughness sub-layer, and hence the model fails to perform well
693 (Weligepolage et al., 2012). The reliance of SEBS on an accurate representation of the surface-
694 air temperature gradient also limits the effectiveness of the model for global application,
695 demanding improvements in characterizing the spatial and temporal representativeness of such
696 variables.

697 It is apparent from Sections 3.2 and 3.3 that the application of gridded data for modelling
698 evaporation inevitably reduces the predictive performance of all models, regardless of their
699 complexity in the evaporation process or their economy in forcing data requirements. In fact,
700 the footprint mismatch between the tower- and grid-based simulations is likely to increase
701 uncertainties in the forcing data and cause discrepancies between the simulated and tower-
702 based evaporation values. Importantly, comparing the models for their relative performance
703 (see Figure 7 and Figure 10) reveals that the performance decrease for grid-based analysis was
704 not equal amongst all of the models. For instance, SEBS was observed to be more sensitive to
705 the use of gridded forcing data, most likely as a result of inconsistencies in temperature

706 gradient fields: an aspect that has been noted previously (van der Kwast et al., 2009; Ershadi et
707 al., 2013). Although input uncertainty also impacts the performance of PT-JPL, PM-Mu and
708 GLEAM, the *NSE* and R^2 of gridded simulations for those models are closer to their tower-based
709 counterparts. Apart from indicating a robust model structure, the reduced impact seen in these
710 schemes may also be a consequence of avoiding the use of forcing data such as land surface
711 temperature and wind speed data, which are known to be uncertain at both the grid and
712 tower-scale. Regardless of the culprit behind the observed performance discrepancy between
713 tower and grid-based simulations, it is clear that some models are better suited to global
714 application than others – at least given the quality of currently available global forcing datasets.

715 Importantly, the results presented in Sections 3.2 and 3.3 showed that evaluating tower or grid-
716 based statistical responses alone is not enough to identify those forcing variables most
717 impacting model performance. Diagnosing forcing sensitivity is not trivial given non-linearities
718 in the models and the high level of interaction within model variables and parameters. Indeed,
719 caution is warranted in any approaches seeking to evaluate evaporation models using gridded
720 data in isolation, as this is likely to yield unreliable performance metrics of the models. It is
721 important to perform a parallel tower-based data assessment to increase confidence in any
722 single models performance (Su et al., 2005) in any evaluation approach, particularly those
723 occurring at global scales.

724 Although the largest possible set of eddy-covariance towers and a common set of forcing data
725 was used to evaluate the different model simulations, there are still inevitable limitations in the
726 evaluations. Identifying such limitations is important not only for the current evaluations, but
727 also in guiding future contributions. One such example relates to the period of tower data used
728 for evaluation in this study (see Figure A1), as the data record length varies amongst the towers
729 and the data are not uniformly distributed across seasons. Moreover, the towers are not evenly
730 distributed across the studied biomes and climate zones (see Figure 1, Table A1), with only one
731 tower covering the entire evergreen broadleaf forest biome and two towers covering the
732 wetland biome. Further, no towers were available for use in arctic and tropical climate zones.
733 Although the tropical climate zone, especially Amazonian forests, is accounted as a critical
734 component in studies of the global water and energy cycles (Chahine, 1992; Wohl et al., 2012),

735 relatively few towers in this zone provide land surface temperature and longwave upward
736 radiation data needed for the SEBS model. An additional limitation is the coarse (8 km) spatial
737 resolution of the GIMMS NDVI data used in the models for the tower-based analysis, as this
738 resolution certainly does not correspond with the footprint of eddy-covariance sensors at any
739 of the towers. Developments towards improving the availability and access to long-term high-
740 resolution Landsat images (e.g. via Google Earth Engine; <https://earthengine.google.org>) might
741 be one way to improve model forcing and evaluation exercises, especially with the
742 development of high-resolution vegetation products (Houborg et al. 2016).

743 While the accuracy of individual variables in the LandFlux dataset were enhanced by bias
744 correction against independent data sources (see Section 2.1), diagnosing the internal
745 consistency of the data fields (McCabe et al., 2008), especially for air temperature, land surface
746 temperature, wind speed and humidity, is a concept that has not received much attention to
747 date and demands more considered investigations and analysis. Internal consistency is an
748 extremely challenging objective, but is critically important for flux estimation, where so many
749 different forcing data are required. Essentially it demands that all required model data are
750 derived from a common set of forcing variables, rather than by the standard approach of
751 compilation based on availability and accessibility. The most illustrative example would be in
752 the development of radiation data, derived here from NASA-GEWEX SRB sources (Stackhouse et
753 al., 2011). Calculation of radiation components requires air temperature, surface temperature,
754 land surface and vegetation features, as well as numerous other elements. However, these
755 underlying variables are rarely if ever retained to provide a consistent overall forcing data set
756 (i.e. the meteorological variables used in producing the SRB data are not subsequently used to
757 drive the models). Interdependencies in forcing affect many variables in the estimation of
758 evaporation, yet products are not developed with this simple consistency principle in mind.
759 Apart from introducing further biases and uncertainties into model simulations, until such
760 consistency is attained, discriminating between the impact of forcing versus the model
761 sensitivity to that forcing will remain extremely challenging.

762 From one perspective, the performance of the evaporation models examined here seems
763 relatively poor, even when they are forced with high-quality tower-based data. PT-JPL, which

764 was identified as one of the most consistent and best performing models, still presented a
765 relative error of 41%, with errors for GLEAM, PM-Mu and SEBS of 43%, 52% and 72%,
766 respectively. However, it is important to recognise that tower-based evaluation represents one
767 of the strictest measure of model performance and comes with its own caveats. One question
768 that remains unanswered is whether it is even appropriate to expect models run with large-
769 scale gridded forcing to replicate the small-scale response observed by eddy-covariance towers.
770 The alternative perspective, given inherent uncertainties in forcing, observations and
771 specification of model parameters, is that these results are encouraging. Broader scale metrics
772 such as hydrological consistency (McCabe et al., 2008), catchment based assessments or water
773 budget closure approaches would provide a better guide (Sheffield et al., 2009) and indeed,
774 such evaluations will need to be performed. These questions highlight the difficulties in not just
775 producing global estimates, but perhaps more importantly, in evaluating their quality.

776 The observed variability of modelling performance across the studied biomes and climate zones
777 implies that caution is required in advocating any single model for large-scale or global
778 application. These results reflect previous findings that any one modelling approach is
779 incapable of accurately reflecting the range of flux responses occurring across diverse
780 landscapes (Ershadi et al., 2014; Ershadi et al., 2015). One possible solution to address this
781 inherent model limitation is to assemble a mosaicked product based on the predictive skill of
782 the model(s) over particular biomes or climate zones. Another approach might be to develop an
783 ensemble product using a suitable multi-model blending technique, such as a Bayesian Model
784 Averaging approach (Hoeting et al., 1999; Yao et al., 2014). Either way, it is clear that further
785 multi-model assessments are required for progressing global scale flux characterisation and to
786 ensure a robust and representative product is developed.

787

788 **5 Conclusions**

789 It is something of a contradiction that the global-scale estimation of surface fluxes is both
790 straightforward and extremely challenging at the same time. It is more straightforward than
791 ever due to the availability of needed forcing data from various sources, such as numerical

792 weather prediction or other operational products, as well as the increased development of
793 global satellite based datasets. However, the comparative ease with which products can be
794 developed belies the difficulties in actually developing robust and coherent simulations.
795 Uncertainties in the use of internally inconsistent forcing data, the influence of untested model
796 parameterizations over different land surface and climate types, violation of model
797 assumptions in their graduation from the local scale to global scale and the perennial question
798 on how to best evaluate model output all seek to confound global flux efforts.

799 The evaluation of four process-based evaporation models as part of the GEWEX LandFlux
800 project undertaken here over a range of biome types and climate zones, highlighted the
801 variable performance and verified the sentiment that no single model is able to consistently
802 outperform any other. While individual model results at the tower scale allowed for a relative
803 performance ranking, the overall model errors when considered globally were high. Of those
804 models assessed here and being considered as potential candidates for a GEWEX LandFlux
805 product, PT-JPL and GLEAM represent the most likely schemes for providing consistent
806 simulation response over a range of biome and climate types. In a challenge for the
807 development of more accurate global flux products, application of gridded data reduces the
808 performance of all models, even if the overall performance ranking does not change between
809 simulation runs. Such a response has obvious implications when model simulations at the
810 continental and global scales are increasingly required in many applications and where not only
811 the forcing data have large uncertainties, but also the underlying assumptions of the models
812 themselves are likely to be questioned. Further investigations on the reasons for such variable
813 performance and ways to offset the inherent uncertainties in global forcing are required.
814 Additional research is also needed to improve the structure and parameterization of some of
815 these candidate models, to understand model sensitivities to forcing (by conducting a thorough
816 sensitivity analysis) and to develop and implement an appropriate ensemble modelling and
817 merging technique that takes advantage of individual model performance over defined regions.
818 Further detailed comparisons against estimates from more complex modelling systems, such as
819 reanalysis and numerical weather prediction models, are needed to provide greater context
820 and additional benchmarking metrics to guide future investigations.

821 **Appendix A: Description of Tower Locations**

822 Table A1: Selected eddy-covariance and their attributes. Further details and information on

823 individual tower sites can be found via the Fluxnet data portal (<http://fluxnet.fluxdata.org/>)

Site-ID	Country	Lat.	Lon.	Ground Elev. (masl)	Tower height (m)	IGBP	Climate Class	Climate Zone	Reference
BW-Ma1	Botswana	-19.9	23.6	947	12.6	WSA	BSh	Dry	(Veenendaal et al., 2004)
CA-Ca1	Canada	49.9	-125.3	324	43	ENF	Cfb	Temperate	(Humphreys et al., 2006)
CA-Mer	Canada	45.4	-75.5	68	3	WET	Dfb	Temperate-Continental	(Kross et al., 2013)
CA-Oas	Canada	53.6	-106.2	594	39	DBF	Dfc	Boreal	(Fu et al., 2014)
CA-Obs	Canada	54.0	-105.1	593	25	ENF	Dfc	Boreal	(Fu et al., 2014)
CA-Ojp	Canada	53.9	-104.7	517	28	ENF	Dfc	Boreal	(Hilton et al., 2014)
CA-Qfo	Canada	49.7	-74.3	389	25	ENF	Dfc	Boreal	(Flanagan et al., 2012)
CN-Do2	China	31.6	121.9	4	5	WET	Cfa	Sub-Tropical	(Yan et al., 2008)
DE-Geb	Germany	51.1	10.9	159	6	CRO	Cfb	Temperate	(Smith et al., 2010)
DE-Hai	Germany	51.1	10.5	458	43.5	DBF	Cfb	Temperate	(Rebmann et al., 2005)
DE-Kli	Germany	50.9	13.5	480	3.5	CRO	Cfb	Temperate	(Smith et al., 2010)
DE-Meh	Germany	51.3	10.7	289	3	GRA	Cfb	Temperate	(Don et al., 2009)
DE-Tha	Germany	51.0	13.6	387	42	ENF	Cfb	Temperate	(Delpierre et al., 2009)
DE-Wet	Germany	50.5	11.5	789	27	ENF	Cfb	Temperate	(Richardson et al., 2010)
FR-LBr	France	44.7	-0.8	71	41	ENF	Cfb	Temperate	(Göckede et al., 2008)
FR-Lam	France	43.5	1.2	182	3.65	CRO	Cfb	Temperate	(Merlin et al., 2011)
FR-Pue	France	43.7	3.6	271	13	EBF	Csa	Sub-Tropical	(Soudani et al., 2014)
IL-Yat	Israel	31.3	35.1	654	18	ENF	BSh	Dry	(Sprintsin et al., 2011)
IT-BCi	Italy	40.5	15.0	9	2	CRO	Csa	Sub-Tropical	(Reichstein et al., 2003)
IT-Col	Italy	41.8	13.6	1534	25	DBF	Cfa	Sub-Tropical	(Chiti et al., 2010)
IT-Lav	Italy	46.0	11.3	1367	33	ENF	Cfb	Temperate	(Stoy et al., 2013)
IT-MBo	Italy	46.0	11.0	1563	2.5	GRA	Cfb	Temperate	(Gamon et al., 2010)
IT-Noe	Italy	40.6	8.2	27	3.6	CSH	Csa	Sub-Tropical	(Carvalhais et al., 2010)
IT-Ro1	Italy	42.4	11.9	174	20	DBF	Csa	Sub-Tropical	(Chiti et al., 2010)
JP-Tom	Japan	42.7	141.5	133	42	MF	Dfb	Temperate-Continental	(Saigusa et al., 2010)
NL-Ca1	Netherlands	52.0	4.9	-1	5	GRA	Cfb	Temperate	(Gioli et al., 2004)
NL-Loo	Netherlands	52.2	5.7	34	27	ENF	Cfb	Temperate	(Sulkava et al., 2011)
PT-Mi2	Portugal	38.5	-8.0	191	2.5	GRA	Csa	Sub-Tropical	(Gilmanov et al., 2007)
RU-Fyo	Russia	56.5	32.9	274	29	ENF	Dfb	Temperate-Continental	(Smith et al., 2010)
SE-Nor	Sweden	60.1	17.5	35	103	ENF	Dfb	Temperate-Continental	(Zierl et al., 2007)

Site-ID	Country	Lat.	Lon.	Ground Elev. (masl)	Tower height (m)	IGBP	Climate Class	Climate Zone	Reference
US-ARM	USA	36.6	-97.5	318	60	CRO	Cfa	Sub-Tropical	(Lokupitiya et al., 2009)
US-Aud	USA	31.6	-110.5	1474	4	GRA	BSk	Dry	(Horn and Schulz, 2011)
US-Bkg	USA	44.3	-96.8	496	4	GRA	Dfa	Temperate-Continental	(Hollinger et al., 2010)
US-Bo1	USA	40.0	-88.3	218	10	CRO	Dfa	Temperate-Continental	(Hollinger et al., 2010)
US-Bo2	USA	40.0	-88.3	220	10	CRO	Dfa	Temperate-Continental	(Hollinger et al., 2010)
US-CaV	USA	39.1	-79.4	993	4	GRA	Cfb	Temperate	(Hollinger et al., 2010)
US-FPe	USA	48.3	-105.1	632	3.5	GRA	BSk	Dry	(Horn and Schulz, 2011)
US-Goo	USA	34.3	-89.9	94	4	GRA	Cfa	Sub-Tropical	(Hollinger et al., 2010)
US-MMS	USA	39.3	-86.4	290	48	DBF	Cfa	Sub-Tropical	(Dragoni et al., 2011)
US-MOz	USA	38.7	-92.2	238	30	DBF	Cfa	Sub-Tropical	(Hollinger et al., 2010)
US-NR1	USA	40.0	-105.5	3053	26	ENF	Dfc	Boreal	(Hilton et al., 2014)
US-SRM	USA	31.8	-110.9	1120	6.4	WSA	BSk	Dry	(Cavanaugh et al., 2011)
US-WCr	USA	45.8	-90.1	524	30	DBF	Dfb	Temperate-Continental	(Curtis et al., 2002)
US-Wkg	USA	31.7	-109.9	1522	6.4	GRA	BSk	Dry	(Scott, 2010)
US-Wrc	USA	45.8	-122.0	391	85	ENF	Csb	Temperate	(Wharton et al., 2009)

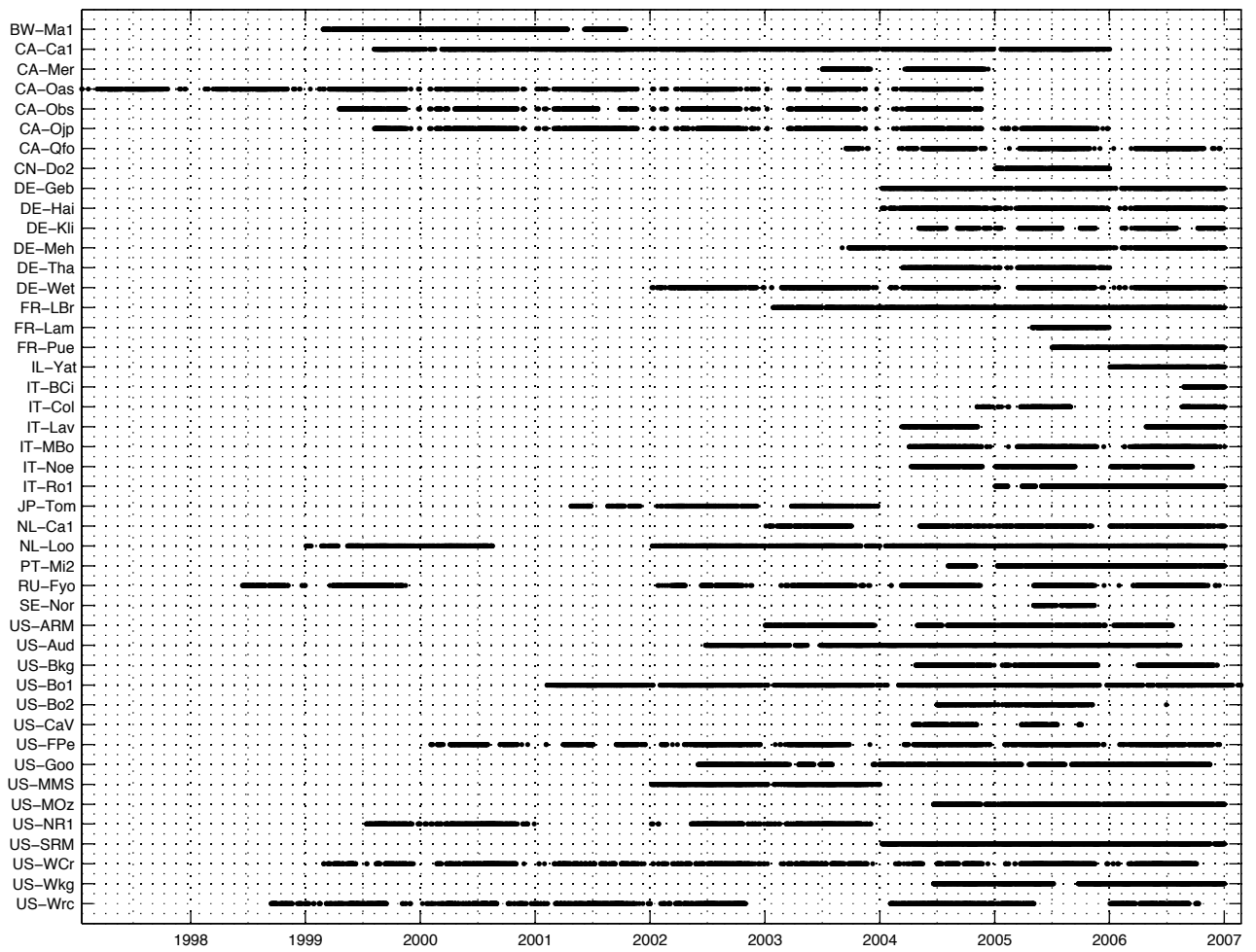
825

826

827 Figure A1: Temporal duration of the eddy-covariance based flux and tower meteorological
828 observations for each of the 45 sites used in this study

829

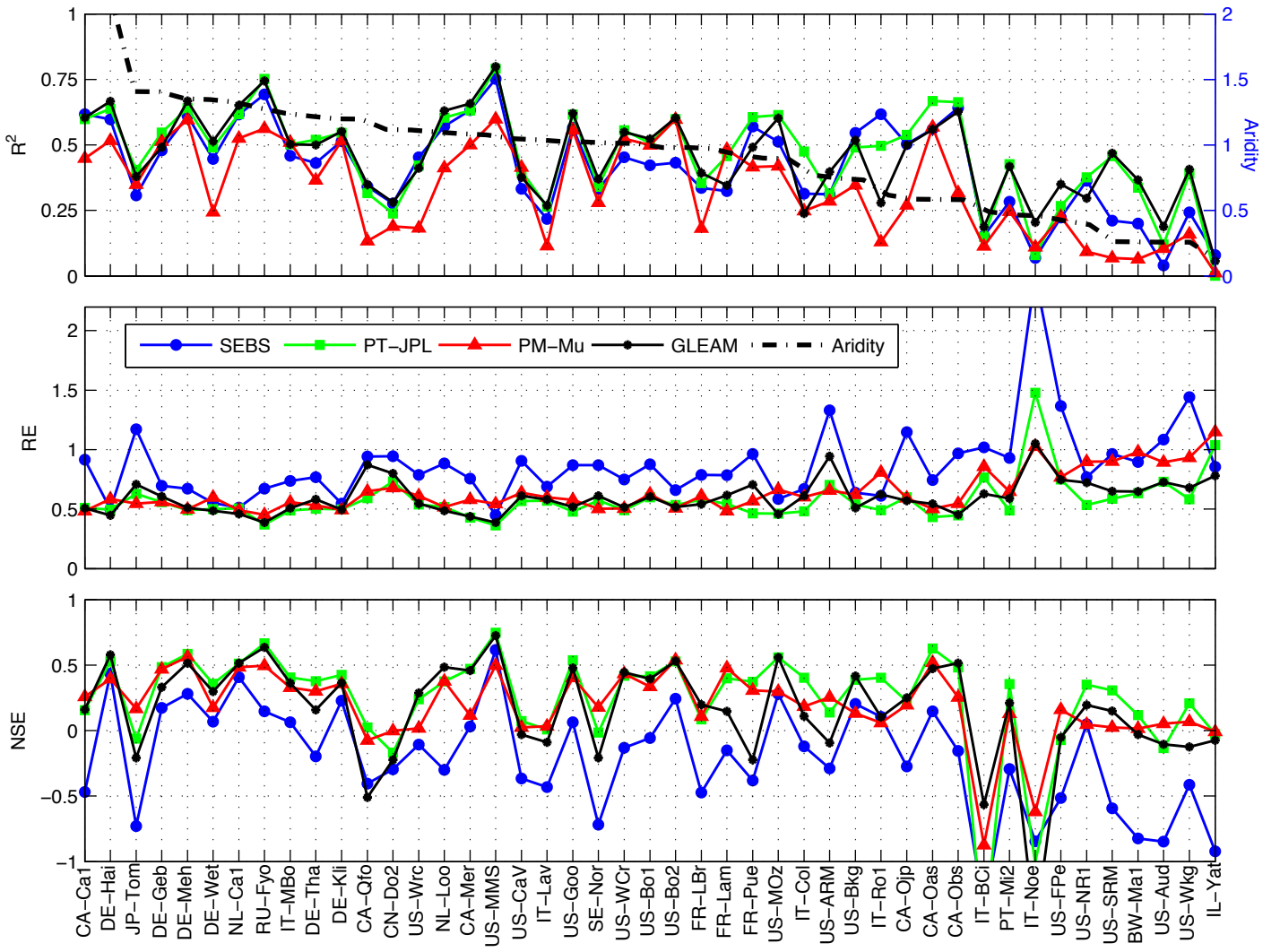
830



831

832 Figure A2: Comparison of the performance skill of the models in reproducing evaporation for
833 the grid-based analyses. R^2 is the coefficient of determination, RE is relative error (lower is
834 better) and NSE is the Nash-Sutcliffe Efficiency (higher is better). Towers are arranged from left
835 to right based on an aridity index (secondary y-axis).

836



837 **Code Availability**

838 The PM-Mu, SEBS and PT-JPL models were coded in MATLAB as part of the GEWEX LandFlux and
839 WACMOS-ET projects, in discussion with (but independent of) the principal model authors, as
840 referenced in the relevant publications. The GLEAM model was developed in MATLAB by Diego Miralles
841 and Brecht Martens. All model code can be made available upon an emailed request to
842 hydrology@kaust.edu.sa, including a brief description of the intended purpose and application.

843 **Data Availability**

844 Evaporation model output presented here for both the gridded and tower based analyses can be
845 provided upon an emailed request to hydrology@kaust.edu.sa. The request should include a brief
846 description of the intended purpose and application of the model data.

847 **Acknowledgements**

848 Research reported in this publication was supported by the King Abdullah University of Science
849 and Technology (KAUST). D.G.M. acknowledges the financial support from The Netherlands
850 Organization for Scientific Research through grant 863.14.004. We appreciate the support of
851 the ESA funded WACMOS-ET project for both fruitful scientific discussions and guidance in
852 ensuring complementarity of these joint efforts. We thank the FLUXNET site investigators for
853 allowing the use of their meteorological data. This work used eddy-covariance data acquired by
854 the FLUXNET community and in particular by the AmeriFlux program (U.S. Department of
855 Energy, Biological and Environmental Research, Terrestrial Carbon Program: DE-FG02-
856 04ER63917 and DE-FG02-04ER63911), AfriFlux, AsiaFlux, CarboAfrica, CarboEuropeIP,
857 CarboItaly, CarboMont, ChinaFlux, Fluxnet-Canada (supported by CFCAS, NSERC, BIOCAP,
858 Environment Canada, and NRCan), GreenGrass, KoFlux, LBA, NECC, TCOS-Siberia, USCCC. We
859 acknowledge the financial support to the eddy-covariance data harmonization provided by
860 CarboEuropeIP, FAO-GTOS-TCO, iLEAPS, Max Planck Institute for Biogeochemistry, National
861 Science Foundation, University of Tuscia, Université Laval and Environment Canada and US
862 Department of Energy and the database development and technical support from Berkeley
863 Water Centre, Lawrence Berkeley National Laboratory, Microsoft Research eScience, Oak Ridge
864 National Laboratory, University of California - Berkeley, University of Virginia.

865

866 **References**

- 867 Adler, R. F., Huffman, G. J., Chang, A., Ferraro, R., Xie, P. P., Janowiak, J., Rudolf, B., Schneider, U., Curtis,
868 S., Bolvin, D., Gruber, A., Susskind, J., Arkin, P., and Nelkin, E.: The version-2 global precipitation
869 climatology project (GPCP) monthly precipitation analysis (1979-present), *Journal of*
870 *Hydrometeorology*, 4, 1147-1167, 2003.
- 871 Allen, R. G.: Using the FAO-56 dual crop coefficient method over an irrigated region as part of an
872 evapotranspiration intercomparison study, *Journal of Hydrology*, 229, 27-41, 2000.
- 873 Allen, R. G., Tasumi, M., and Trezza, R.: Satellite-Based Energy Balance for Mapping Evapotranspiration
874 with Internalized Calibration (METRIC)-Model, *Journal of Irrigation and Drainage Engineering*, 133,
875 380-394, 2007.
- 876 Armstrong, R. L., Brodzik, M. J., Knowles, K., and Savoie, M.: Global monthly EASE-Grid snow water
877 equivalent climatology, Boulder, CO: National Snow and Ice Data Center, Digital media, 2005.
878 2005.
- 879 Badgley, G., Fisher, J. B., Jiménez, C., Tu, K. P., and Vinukollu, R.: On uncertainty in global terrestrial
880 evapotranspiration estimates from choice of input forcing datasets, *Journal of Hydrometeorology*,
881 doi: 10.1175/JHM-D-14-0040.1, 2015. 2015.
- 882 Baldocchi, D., Falge, E., Gu, L., Olson, R., Hollinger, D., Running, S., Anthoni, P., Bernhofer, C., Davis, K.,
883 Evans, R., Fuentes, J., Goldstein, A., Katul, G., Law, B., Lee, X., Malhi, Y., Meyers, T., Munger, W.,
884 Oechel, W., Paw, K. T., Pilegaard, K., Schmid, H. P., Valentini, R., Verma, S., Vesala, T., Wilson, K.,
885 and Wofsy, S.: FLUXNET: A New Tool to Study the Temporal and Spatial Variability of Ecosystem-
886 Scale Carbon Dioxide, Water Vapor, and Energy Flux Densities, *Bulletin of the American*
887 *Meteorological Society*, 82, 2415-2434, 2001.
- 888 Bastiaanssen, W. G. M., Menenti, M., Feddes, R. A., and Holtslag, A. A. M.: A remote sensing surface
889 energy balance algorithm for land (SEBAL). 1. Formulation, *Journal of Hydrology*, 212-213, 198-
890 212, 1998.
- 891 Bos, M. G., Kselik, R. A. L., Allen, R. G., and Molden, D. J.: *Water Requirements for Irrigation and the*
892 *Environment*, Springer, Dordrecht, 2008.
- 893 Bouchet, R. J.: Evapotranspiration réelle et potentielle, signification climatique. General Assembly
894 Berkeley, International Association for Hydrological Sciences. Gentbrugge, Belgium. **62**: 134-142,
895 1963.

896 Brutsaert, W.: Evaporation Into the Atmosphere : theory, history, and applications, Reidel Publishing,
897 Dordrecht etc., 1982.

898 Brutsaert, W.: Hydrology : An Introduction, Cambridge University Press, Cambridge, 2005.

899 Brutsaert, W. and Stricker, H.: An advection-aridity approach to estimate actual regional
900 evapotranspiration, Water Resour. Res., 15, 443-450, 1979.

901 Carvalhais, N., Reichstein, M., Collatz, G. J., Mahecha, M. D., Migliavacca, M., Neigh, C. S. R., Tomelleri,
902 E., Benali, A. A., Papale, D., and Seixas, J.: Deciphering the components of regional net ecosystem
903 fluxes following a bottom-up approach for the Iberian Peninsula, Biogeosciences, 7, 3707-3729,
904 2010.

905 Cavanaugh, M. L., Kurc, S. A., and Scott, R. L.: Evapotranspiration partitioning in semiarid shrubland
906 ecosystems: a two - site evaluation of soil moisture control on transpiration, Ecohydrology, 4,
907 671-681, 2011.

908 Chahine, M. T.: The hydrological cycle and its influence on climate, Nature, 359, 373-380, 1992.

909 Chen, X., Su, Z., Ma, Y., Yang, K., Wen, J., and Zhang, Y.: An Improvement of Roughness Height
910 Parameterization of the Surface Energy Balance System (SEBS) over the Tibetan Plateau, Journal
911 of Applied Meteorology and Climatology, 52, 607-622, 2012.

912 Chiti, T., Papale, D., Smith, P., Dalmonech, D., Matteucci, G., Yeluripati, J., Rodeghiero, M., and Valentini,
913 R.: Predicting changes in soil organic carbon in mediterranean and alpine forests during the Kyoto
914 Protocol commitment periods using the CENTURY model, Soil use and management, 26, 475-484,
915 2010.

916 Coccia, G., Siemann, A., Pan, M., and Wood, E. F.: Creating consistent datasets by combining remotely-
917 sensed data and land surface model estimates through Bayesian uncertainty post-processing: the
918 case of Land Surface Temperature from HIRS, Remote Sensing of Environment, 170, 290-305,
919 doi:10.1016/j.rse.2015.09.010, 2015.

920 Curtis, P. S., Hanson, P. J., Bolstad, P., Barford, C., Randolph, J. C., Schmid, H. P., and Wilson, K. B.:
921 Biometric and eddy-covariance based estimates of annual carbon storage in five eastern North
922 American deciduous forests, Agricultural and Forest Meteorology, 113, 3-19, 2002.

923 Delpierre, N., Soudani, K., Francois, C., Köstner, B., Pontailier, J. Y., Nikinmaa, E., Misson, L., Aubinet, M.,
924 Bernhofer, C., and Granier, A.: Exceptional carbon uptake in European forests during the warm
925 spring of 2007: a data–model analysis, *Global Change Biology*, 15, 1455-1474, 2009.

926 Don, A., Rebmann, C., Kolle, O., Scherer - Lorenzen, M., and Schulze, E. D.: Impact of afforestation -
927 associated management changes on the carbon balance of grassland, *Global Change Biology*, 15,
928 1990-2002, 2009.

929 Douville, H., Ribes, A., Decharme, B., Alkama, R., and Sheffield, J.: Anthropogenic influence on
930 multidecadal changes in reconstructed global evapotranspiration, *Nature Clim. Change*, 3, 59-62,
931 2013.

932 Dragoni, D., Schmid, H. P., Wayson, C. A., Potter, H., Grimmond, C. S. B., and Randolph, J. C.: Evidence of
933 increased net ecosystem productivity associated with a longer vegetated season in a deciduous
934 forest in south - central Indiana, USA, *Global Change Biology*, 17, 886-897, 2011.

935 Ershadi, A., McCabe, M. F., Evans, J. P., Chaney, N. W., and Wood, E. F.: Multi-site evaluation of
936 terrestrial evaporation models using FLUXNET data, *Agricultural and Forest Meteorology*, 187, 46-
937 61, 2014.

938 Ershadi, A., McCabe, M. F., Evans, J. P., Mariethoz, G., and Kavetski, D.: A Bayesian analysis of sensible
939 heat flux estimation: Quantifying uncertainty in meteorological forcing to improve model
940 prediction, *Water Resources Research*, 49, 2343-2358, 2013.

941 Ershadi, A., McCabe, M. F., Evans, J. P., and Wood, E. F.: Impact of model structure and parameterization
942 on Penman–Monteith type evaporation models, *Journal of Hydrology*, 525, 521-535, 2015.

943 Famiglietti, J. S., Lo, M., Ho, S. L., Bethune, J., Anderson, K. J., Syed, T. H., Swenson, S. C., de Linage, C. R.,
944 and Rodell, M.: Satellites measure recent rates of groundwater depletion in California's Central
945 Valley, *Geophysical Research Letters*, 38(3), 10.1029/2010GL046442, 2011.

946 Fisher, J. B., Tu, K. P., and Baldocchi, D. D.: Global estimates of the land-atmosphere water flux based on
947 monthly AVHRR and ISLSCP-II data, validated at 16 FLUXNET sites, *Remote Sensing of
948 Environment*, 112, 901-919, 2008.

949 Flanagan, L. B., Cai, T., Black, T. A., Barr, A. G., McCaughey, J. H., and Margolis, H. A.: Measuring and
950 modeling ecosystem photosynthesis and the carbon isotope composition of ecosystem-respired
951 CO₂ in three boreal coniferous forests, *Agricultural and Forest Meteorology*, 153, 165-176, 2012.

952 Fu, D., Chen, B., Zhang, H., Wang, J., Black, T. A., Amiro, B. D., Bohrer, G., Bolstad, P., Coulter, R., and
953 Rahman, A. F.: Estimating landscape net ecosystem exchange at high spatial–temporal resolution
954 based on Landsat data, an improved upscaling model framework, and eddy covariance flux
955 measurements, *Remote Sensing of Environment*, 141, 90-104, 2014.

956 Gamon, J. A., Coburn, C., Flanagan, L. B., Huemmrich, K. F., Kiddle, C., Sanchez-Azofeifa, G. A., Thayer, D.
957 R., Vescovo, L., Gianelle, D., and Sims, D. A.: SpecNet revisited: bridging flux and remote sensing
958 communities, *Can. J. Remote Sens.*, 36, S376-S390, 2010.

959 Gash, J. H.: An analytical model of rainfall interception by forests quarterly, *Journal of Royal*
960 *Meteorological Society*, 105, 43-45, 1979.

961 Gilmanov, T., Soussana, J., Aires, L., Allard, V., Ammann, C., Balzarolo, M., Barcza, Z., Bernhofer, C.,
962 Campbell, C., Cernusca, A., Cescatti, A., Clifton-Brown, J., Dirks, B., Dore, S., Eugster, W., Fuhrer, J.,
963 Gimeno, C., Gruenwald, T., Haszpra, L., Hensen, A., Ibrom, A., Jacobs, A., Jones, M., Lanigan, G.,
964 Laurila, T., Lohila, A., Manca, G., Marcolla, B., Nagy, Z., Pilegaard, K., Pinter, K., Pio, C., Raschi, A.,
965 Rogiers, N., Sanz, M., Stefani, P., Sutton, M., Tuba, Z., Valentini, R., Williams, M., and Wohlfahrt,
966 G.: Partitioning European grassland net ecosystem CO₂ exchange into gross primary productivity
967 and ecosystem respiration using light response function analysis, *Agriculture, Ecosystems and*
968 *Environment*, 121, 93 - 120, 2007.

969 Gioli, B., Miglietta, F., De Martino, B., Hutjes, R. W. A., Dolman, H. A. J., Lindroth, A., Schumacher, M.,
970 Sanz, M. J., Manca, G., and Peressotti, A.: Comparison between tower and aircraft-based eddy
971 covariance fluxes in five European regions, *Agricultural and Forest Meteorology*, 127, 1-16, 2004.

972 Göckede, M., Foken, T., Aubinet, M., Aurela, M., Banza, J., Bernhofer, C., Bonnefond, J.-M., Brunet, Y.,
973 Carrara, A., and Clement, R.: Quality control of CarboEurope flux data–Part 1: Coupling footprint
974 analyses with flux data quality assessment to evaluate sites in forest ecosystems, *Biogeosciences*,
975 5, 433-450, 2008.

976 Granger, R. J.: Satellite-derived estimates of evapotranspiration in the Gediz basin, *Journal of Hydrology*,
977 229, 70-76, 2000.

978 Greve, P., Orlowsky, B., Mueller, B., Sheffield, J., Reichstein, M., and Seneviratne, S. I.: Global assessment
979 of trends in wetting and drying over land, *Nature geoscience*, 7, 716-721, 2014.

980 Guillod, B. P., Orlowsky, B., Miralles, D. G., Teuling, A. J., and Seneviratne, S. I.: Reconciling spatial and
981 temporal soil moisture effects on afternoon rainfall, *Nat Commun*, 6, 2015.

982 Hansen, M. C., Townshend, J. R. G., DeFries, R. S., and Carroll, M.: Estimation of tree cover using MODIS
983 data at global, continental and regional/local scales, *Int. J. Remote Sens.*, 26, 4359-4380, 2005.

984 Harman, I.: The Role of Roughness Sublayer Dynamics Within Surface Exchange Schemes, *Boundary-*
985 *Layer Meteorology*, 142, 1-20, 2012.

986 Hilton, T. W., Davis, K. J., and Keller, K.: Evaluating terrestrial CO₂ flux diagnoses and uncertainties from
987 a simple land surface model and its residuals, *Biogeosciences*, 11, 217-235, 2014.

988 Hirschi, M., Seneviratne, S. I., Alexandrov, V., Boberg, F., Boroneant, C., Christensen, O. B., Formayer, H.,
989 Orłowsky, B., and Stepanek, P.: Observational evidence for soil-moisture impact on hot extremes
990 in southeastern Europe, *Nature Geoscience*, 4, 17-21, 2011.

991 Hoeting, J. A., Madigan, D., Raftery, A. E., and Volinsky, C. T.: Bayesian Model Averaging: A Tutorial,
992 *Statistical Science*, 14, 382-401, 1999.

993 Hollinger, D. Y., Ollinger, S. V., Richardson, A. D., Meyers, T. P., Dail, D. B., Martin, M. E., Scott, N. A.,
994 Arkebauer, T. J., Baldocchi, D. D., and Clark, K. L.: Albedo estimates for land surface models and
995 support for a new paradigm based on foliage nitrogen concentration, *Global Change Biology*, 16,
996 696-710, 2010.

997 Horn, J. E. and Schulz, K.: Identification of a general light use efficiency model for gross primary
998 production, *Biogeosciences*, 8, 999 - 1021, 2011.

999 Houborg, R., McCabe, M. F., and Gao, F.: A Spatio-Temporal Enhancement Method for medium
1000 resolution LAI (STEM-LAI), *International Journal of Applied Earth Observation and Geoinformation*,
1001 47, 15-29, 2016.

1002 Huffman, G. J., Adler, R. F., Rudolph, B., Schneider, U., and Keehn, P.: Global precipitation estimates
1003 based on a technique for combining satellite-based estimates, rain gauge analysis, and NWP
1004 model precipitation information, *J. Climate*, 8, 1284-1295, 1995.

1005 Humphreys, E. R., Black, T. A., Morgenstern, K., Cai, T., Drewitt, G. B., Nesic, Z., and Trofymow, J. A.:
1006 Carbon dioxide fluxes in coastal Douglas-fir stands at different stages of development after
1007 clearcut harvesting, *Agricultural and Forest Meteorology*, 140, 6-22, 2006.

1008 Jiménez, C., Prigent, C., Mueller, B., Seneviratne, S. I., McCabe, M. F., Wood, E. F., Rossow, W. B.,
1009 Balsamo, G., Betts, A. K., Dirmeyer, P. A., Fisher, J. B., Jung, M., Kanamitsu, M., Reichle, R. H.,

1010 Reichstein, M., Rodell, M., Sheffield, J., Tu, K., and Wang, K.: Global intercomparison of 12 land
1011 surface heat flux estimates, *J. Geophys. Res.*, 116, D02102, 2011.

1012 Jiménez-Muñoz, J., Sobrino, J., Plaza, A., Guanter, L., Moreno, J., and Martínez, P.: Comparison Between
1013 Fractional Vegetation Cover Retrievals from Vegetation Indices and Spectral Mixture Analysis:
1014 Case Study of PROBA/CHRIS Data Over an Agricultural Area, *Sensors*, 9, 768-793, 2009.

1015 Jung, M., Reichstein, M., Ciais, P., Seneviratne, S. I., Sheffield, J., Goulden, M. L., Bonan, G., Cescatti, A.,
1016 Chen, J., and de Jeu, R.: Recent decline in the global land evapotranspiration trend due to limited
1017 moisture supply, *Nature*, 467, 951-954, 2010.

1018 Kross, A., Seaquist, J. W., Roulet, N. T., Fernandes, R., and Sonnentag, O.: Estimating carbon dioxide
1019 exchange rates at contrasting northern peatlands using MODIS satellite data, *Remote Sensing of
1020 Environment*, 137, 234-243, 2013.

1021 Kustas, W. P., Perry, E. M., Doraiswamy, P. C., and Moran, M. S.: Using satellite remote sensing to
1022 extrapolate evapotranspiration in time and space over a semiarid rangeland, *Remote Sens.
1023 Environ.*, 49, 275-286, 1994.

1024 Liu, Y. Y., de Jeu, R. A. M., McCabe, M. F., Evans, J. P., and van Dijk, A. I. J. M.: Global long-term passive
1025 microwave satellite-based retrievals of vegetation optical depth, *Geophys. Res. Lett.*, 38, L18402,
1026 2011a.

1027 Liu, Y. Y., Dorigo, W. A., Parinussa, R. M., De Jeu, R. A. M., Wagner, W., McCabe, M. F., Evans, J. P., and
1028 Van Dijk, A. I. J. M.: Trend-preserving blending of passive and active microwave soil moisture
1029 retrievals, *Remote Sensing of Environment*, 123, 280-297, 2012.

1030 Liu, Y. Y., Parinussa, R. M., Dorigo, W. A., De Jeu, R. A. M., Wagner, W., M. Van Dijk, A. I. J., McCabe, M.
1031 F., and Evans, J. P.: Developing an improved soil moisture dataset by blending passive and active
1032 microwave satellite-based retrievals, *Hydrol. Earth Syst. Sci.*, 15, 425-436, 2011b.

1033 Liu, Y. Y., van Dijk, A. I. J. M., McCabe, M. F., Evans, J. P., and de Jeu, R. A. M.: Global vegetation biomass
1034 change (1988-2008) and attribution to environmental and human drivers, *Global Ecology and
1035 Biogeography*, 22, 692-705, 2013.

1036 Lokupitiya, E., Denning, S., Paustian, K., Baker, I., Schaefer, K., VERMA, S., MEYERS, T., Bernacchi, C. J.,
1037 SUYKER, A., and Fischer, M.: Incorporation of crop phenology in Simple Biosphere Model (SiBcrop)

1038 to improve land-atmosphere carbon exchanges from croplands, *Biogeosciences*, 6, 1103 - 1103,
1039 2009.

1040 Luoju, K., Pulliainen, J., Takala, M., Lemmetyinen, J., Derksen, C., and Wang, L.: Snow water equivalent
1041 (SWE) product guide, *Global Snow Monitoring for Climate Research*, 1, 2010.

1042

1043 Mach, D. M., Christian, H. J., Blakeslee, R. J., Boccippio, D. J., Goodman, S. J., and Boeck, W. L.:
1044 Performance assessment of the optical transient detector and lightning imaging sensor, *Journal of*
1045 *Geophysical Research: Atmospheres (1984–2012)*, 112, 2007.

1046 McCabe, M. F. and Wood, E. F.: Scale influences on the remote estimation of evapotranspiration using
1047 multiple satellite sensors, *Remote Sensing of Environment*, 105, 271-285, 2006.

1048 McCabe, M. F., Wood, E. F., Wójcik, R., Pan, M., Sheffield, J., Gao, H., and Su, H.: Hydrological
1049 consistency using multi-sensor remote sensing data for water and energy cycle studies, *Remote*
1050 *Sensing of Environment*, 112, 430-444, 2008.

1051 Merlin, O., Al Bitar, A., Rivalland, V., Béziat, P., Ceschia, E., and Dedieu, G.: An analytical model of
1052 evaporation efficiency for unsaturated soil surfaces with an arbitrary thickness, *Journal of Applied*
1053 *Meteorology and Climatology*, 50, 457-471, 2011.

1054 Michel, D., Jiménez C., Miralles D. G., Jung M., Hirschi M., Ershadi A., Martens B., McCabe M. F., Fisher J.
1055 B., Mu Q., Seneviratne S. I., Wood E. F. and Fernández-Prieto D.: The WACMOS-ET project – Part
1056 1: Tower-scale evaluation of four remote sensing-based evapotranspiration algorithms, *Hydrol.*
1057 *Earth Syst. Sci. Discuss.*, 12(10): 10739-10787, 2015

1058 Miralles, D. G., De Jeu, R. A. M., Gash, J. H., Holmes, T. R. H., and Dolman, A. J.: Magnitude and variability
1059 of land evaporation and its components at the global scale, *Hydrol. Earth Syst. Sci.*, 15, 967-981,
1060 2011a.

1061 Miralles, D. G., Gash, J. H., Holmes, T. R. H., de Jeu, R. A. M., and Dolman, A.: Global canopy interception
1062 from satellite observations, *Journal of Geophysical Research*, 115, D16122, 2010.

1063 Miralles, D. G., Holmes, T. R. H., De Jeu, R. A. M., Gash, J. H., Meesters, A. G. C. A., and Dolman, A. J.:
1064 Global land-surface evaporation estimated from satellite-based observations, *Hydrol. Earth Syst.*
1065 *Sci.*, 15, 453-469, 2011b.

1066 Miralles, D. G., Teuling, A. J., van Heerwaarden, C. C., and de Arellano, J. V.-G.: Mega-heatwave
1067 temperatures due to combined soil desiccation and atmospheric heat accumulation, *Nature*
1068 *Geoscience*, 7, 345-349, 2014a.

1069 Miralles, D. G., van den Berg, M. J., Gash, J. H., Parinussa, R. M., de Jeu, R. A. M., Beck, H. E., Holmes, T.
1070 R. H., Jiménez, C., Verhoest, N. E. C., and Dorigo, W. A.: El Niño–La Niña cycle and recent trends in
1071 continental evaporation, *Nature Climate Change*, 4, 122-126, 2014b.

1072 Miralles, D. G., Jiménez C., Jung M., Michel D., Ershadi A., McCabe M. F., Hirschi M., Martens B., Dolman
1073 A. J., Fisher J. B., Mu Q., Seneviratne S. I., Wood E. F. and Fernández-Prieto D.: The WACMOS-ET
1074 project – Part 2: Evaluation of global terrestrial evaporation data sets, *Hydrol. Earth Syst. Sci.*
1075 *Discuss.*, 12(10): 10651-10700, 2015

1076 Monteith, J. L.: Evaporation and environment, *Symp. Soc. Exp. Biol.*, 19, 205-234, 1965.

1077 Mu, Q., Heinsch, F. A., Zhao, M., and Running, S. W.: Development of a global evapotranspiration
1078 algorithm based on MODIS and global meteorology data, *Remote Sensing of Environment*, 111,
1079 519-536, 2007.

1080 Mu, Q., Zhao, M., Kimball, J. S., McDowell, N. G., and Running, S. W.: A Remotely Sensed Global
1081 Terrestrial Drought Severity Index, *Bulletin of the American Meteorological Society*, 94, 83-98,
1082 2012.

1083 Mu, Q., Zhao, M., and Running, S. W.: Improvements to a MODIS global terrestrial evapotranspiration
1084 algorithm, *Remote Sensing of Environment*, 115, 1781-1800, 2011.

1085 Mu, Q., Zhao, M., and Running, S. W.: MODIS Global Terrestrial Evapotranspiration (ET) Product (NASA
1086 MOD16A2/A3), Algorithm Theoretical Basis Document, Collection, 5, 2013.

1087 Mueller, B., Hirschi, M., Jimenez, C., Ciais, P., Dirmeyer, P. A., Dolman, A. J., Fisher, J. B., Jung, M.,
1088 Ludwig, F., Maignan, F., Miralles, D., McCabe, M. F., Reichstein, M., Sheffield, J., Wang, K. C.,
1089 Wood, E. F., Zhang, Y., and Seneviratne, S. I.: Benchmark products for land evapotranspiration:
1090 LandFlux-EVAL multi-dataset synthesis, *Hydrol. Earth Syst. Sci. Discuss.*, 10, 769-805, 2013.

1091 Mueller, B., Seneviratne, S. I., Jimenez, C., Corti, T., Hirschi, M., Balsamo, G., Ciais, P., Dirmeyer, P.,
1092 Fisher, J. B., Guo, Z., Jung, M., Maignan, F., McCabe, M. F., Reichle, R., Reichstein, M., Rodell, M.,
1093 Sheffield, J., Teuling, A. J., Wang, K., Wood, E. F., and Zhang, Y.: Evaluation of global observations-

1094 based evapotranspiration datasets and IPCC AR4 simulations, *Geophysical Research Letters*, 38,
1095 2011.

1096 Nash, J. E. and Sutcliffe, J. V.: River flow forecasting through conceptual models: Part I - a discussion of
1097 principles, *Journal of Hydrology*, 10, 282-290, 1970.

1098 Nesbitt, S. W., Zipser, E. J., and Kummerow, C. D.: An examination of version-5 rainfall estimates from
1099 the TRMM Microwave Imager, precipitation radar, and rain gauges on global, regional, and storm
1100 scales, *J. Appl. Meteorol.*, 43, 1016-1036, 2004.

1101 Norman, J. M., Kustas, W. P., and Humes, K. S.: Source approach for estimating soil and vegetation
1102 energy fluxes in observations of directional radiometric surface temperature, *Agricultural and
1103 Forest Meteorology*, 77, 263-293, 1995.

1104

1105 Otkin, J. A., Anderson, M. C., Hain, C., and Svoboda, M.: Examining the Relationship between Drought
1106 Development and Rapid Changes in the Evaporative Stress Index, *Journal of Hydrometeorology*,
1107 15, 938-956, 2014.

1108 Penman, H. L.: Natural Evaporation from Open Water, Bare Soil and Grass, *Proceedings of the Royal
1109 Society of London. Series A. Mathematical and Physical Sciences*, 193, 120-145, 1948.

1110 Potter, C. S., Randerson, J. T., Field, C. B., Matson, P. A., Vitousek, P. M., Mooney, H. A., and Klooster, S.
1111 A.: Terrestrial ecosystem production: a process model based on global satellite and surface data,
1112 *Global Biogeochemical Cycles*, 7, 811-841, 1993.

1113 Priestley, C. H. B. and Taylor, R. J.: On the Assessment of Surface Heat Flux and Evaporation Using Large-
1114 Scale Parameters, *Mon. Weather Rev.*, 100, 81-92, 1972.

1115 Rebmann, C., Göckede, M., Foken, T., Aubinet, M., Aurela, M., Berbigier, P., Bernhofer, C., Buchmann,
1116 N., Carrara, A., and Cescatti, A.: Quality analysis applied on eddy covariance measurements at
1117 complex forest sites using footprint modelling, *Theor Appl Climatol*, 80, 121-141, 2005.

1118 Reichstein, M., Rey, A., Freibauer, A., Tenhunen, J., Valentini, R., Banza, J., Casals, P., Cheng, Y.,
1119 Grünzweig, J. M., and Irvine, J.: Modeling temporal and large - scale spatial variability of soil
1120 respiration from soil water availability, temperature and vegetation productivity indices, *Global
1121 biogeochemical cycles*, 17, 2003.

1122 Richardson, A. D., Black, T. A., Ciais, P., Delbart, N., Friedl, M. A., Gobron, N., Hollinger, D. Y., Kutsch, W.
1123 L., Longdoz, B., and Luysaert, S.: Influence of spring and autumn phenological transitions on
1124 forest ecosystem productivity, *Philosophical Transactions of the Royal Society B: Biological*
1125 *Sciences*, 365, 3227-3246, 2010.

1126 Richey, A. S., Thomas, B. F., Lo, M.-H., Reager, J. T., Famiglietti, J. S., Voss, K., Swenson, S., and Rodell,
1127 M.: Quantifying renewable groundwater stress with GRACE, *Water Resources Research*, doi:
1128 10.1002/2015WR017349, 2015. n/a-n/a, 2015.

1129 Rubel, F. and Kottek M.: Observed and projected climate shifts 1901-2100 depicted by world maps of
1130 the Köppen-Geiger climate classification, *Meteorologische Zeitschrift*, 19(2): 135-141, 2010.

1131 Saha, S., Moorthi, S., Pan, H.-L., Wu, X., Wang, J., Nadiga, S., Tripp, P., Kistler, R., Woollen, J., and
1132 Behringer, D.: The NCEP climate forecast system reanalysis, *Bulletin of the American*
1133 *Meteorological Society*, 91, 1015-1057, 2010.

1134 Sahoo, A. K., Pan, M., Troy, T. J., Vinukollu, R. K., Sheffield, J., and Wood, E. F.: Reconciling the global
1135 terrestrial water budget using satellite remote sensing, *Remote Sensing of Environment*, 115,
1136 1850-1865, 2011.

1137 Saigusa, N., Ichii, K., Murakami, H., Hirata, R., Asanuma, J., Den, H., Han, S. J., Ide, R., Li, S. G., and Ohta,
1138 T.: Impact of meteorological anomalies in the 2003 summer on Gross Primary Productivity in East
1139 Asia, *Biogeosciences*, 7, 641-655, 2010.

1140 Scott, R. L.: Using watershed water balance to evaluate the accuracy of eddy covariance evaporation
1141 measurements for three semiarid ecosystems, *Agricultural and Forest Meteorology*, 150, 219-225,
1142 2010.

1143 Sheffield, J., Ferguson, C. R., Troy, T. J., Wood, E. F., and McCabe, M. F.: Closing the terrestrial water
1144 budget from satellite remote sensing, *Geophysical Research Letters*, 36, n/a-n/a, 2009.

1145 Sheffield, J., Wood, E. F., and Munoz-Arriola, F.: Long-term regional estimates of evapotranspiration for
1146 Mexico based on downscaled ISCCP data, *Journal of Hydrometeorology*, 11, 253-275, 2010.

1147 Shuttleworth, W. J. and Wallace, J. S.: Evaporation from sparse crops-an energy combination theory, *Q.*
1148 *J. R. Meteorol. Soc.*, 111, 839-855, 1985.

1149 Simard, M., Pinto, N., Fisher, J. B., and Baccini, A.: Mapping forest canopy height globally with
1150 spaceborne lidar, *Journal of Geophysical Research: Biogeosciences*, 116, G04021, 2011.

1151 Smith, P., Lanigan, G., Kutsch, W. L., Buchmann, N., Eugster, W., Aubinet, M., Ceschia, E., Béziat, P.,
1152 Yeluripati, J. B., and Osborne, B.: Measurements necessary for assessing the net ecosystem carbon
1153 budget of croplands, *Agriculture, ecosystems & environment*, 139, 302-315, 2010.

1154 Sobrino, J. A., Jiménez-Muñoz, J. C., and Paolini, L.: Land surface temperature retrieval from LANDSAT
1155 TM 5, *Remote Sensing of Environment*, 90, 434-440, 2004.

1156 Soudani, K., Hmimina, G., Dufrêne, E., Berveiller, D., Delpierre, N., Ourcival, J.-M., Rambal, S., and Joffre,
1157 R.: Relationships between photochemical reflectance index and light-use efficiency in deciduous
1158 and evergreen broadleaf forests, *Remote Sensing of Environment*, 144, 73-84, 2014.

1159 Sprintsin, M., Cohen, S., Maseyk, K., Rotenberg, E., Grünzweig, J., Karnieli, A., Berliner, P., and Yakir, D.:
1160 Long term and seasonal courses of leaf area index in a semi-arid forest plantation, *Agricultural and
1161 Forest Meteorology*, 151, 565-574, 2011.

1162 Stackhouse, P. W., Gupta, S. K., Cox, S. J., Zhang, T., Mikovitz, J. C., and Hinkelman, L. M.: The
1163 NASA/GEWEX surface radiation budget release 3.0: 24.5-year dataset, *GEWEX News*, 21, 10-12,
1164 2011.

1165 Stoy, P. C., Mauder, M., Foken, T., Marcolla, B., Boegh, E., Ibrom, A., Arain, M. A., Arneth, A., Aurela, M.,
1166 and Bernhofer, C.: A data-driven analysis of energy balance closure across FLUXNET research sites:
1167 The role of landscape scale heterogeneity, *Agricultural and forest meteorology*, 171, 137-152,
1168 2013.

1169 Su, H., McCabe, M. F., Wood, E. F., Su, Z., and Prueger, J. H.: Modeling evapotranspiration during
1170 SMACEX: Comparing two approaches for local- and regional-scale prediction, *Journal of
1171 Hydrometeorology*, 6, 910-922, 2005.

1172 Su, Z.: The Surface Energy Balance System (SEBS) for estimation of turbulent heat fluxes, *Hydrol. Earth
1173 Syst. Sci.*, 6, 85-100, 2002.

1174 Sulkava, M., Luyssaert, S., Zhehle, S., and Papale, D.: Assessing and improving the representativeness of
1175 monitoring networks: The European flux tower network example, *Journal of Geophysical
1176 Research*, 116, 2011.

1177 Tucker, C. J., Pinzon, J. E., Brown, M. E., Slayback, D. A., Pak, E. W., Mahoney, R., Vermote, E. F., and El
1178 Saleous, N.: An extended AVHRR 8 - km NDVI dataset compatible with MODIS and SPOT
1179 vegetation NDVI data, *Int. J. Remote Sens.*, 26, 4485-4498, 2005.

1180 van der Kwast, J., Timmermans, W., Gieske, A., Su, Z., Oliosio, A., Jia, L., Elbers, J., Karssenber, D., and de
1181 Jong, S.: Evaluation of the Surface Energy Balance System (SEBS) applied to ASTER imagery with
1182 flux-measurements at the SPARC 2004 site (Barrax, Spain), *Hydrol. Earth Syst. Sci.*, 13, 1337-1347,
1183 2009.

1184 Veenendaal, M., Kolle, O., and Lloyd, J.: Seasonal variation in energy fluxes and carbon dioxide exchange
1185 for a broad leaved semi-arid savanna (Mopane woodland) in Southern Africa, *Global Change*
1186 *Biology*, 10, 318 - 328, 2004.

1187 Vinukollu, R. K., Sheffield, J., Wood, E. F., Bosilovich, M. G., and Mocko, D.: Multimodel Analysis of
1188 Energy and Water Fluxes: Intercomparisons between Operational Analyses, a Land Surface Model,
1189 and Remote Sensing, *Journal of Hydrometeorology*, 13, 3-26, 2011a.

1190 Vinukollu, R. K., Wood, E. F., Ferguson, C. R., and Fisher, J. B.: Global estimates of evapotranspiration for
1191 climate studies using multi-sensor remote sensing data: Evaluation of three process-based
1192 approaches, *Remote Sensing of Environment*, 115, 801-823, 2011b.

1193 Weligepolage, K., Gieske, A. S. M., van der Tol, C., Timmermans, J., and Su, Z.: Effect of sub-layer
1194 corrections on the roughness parameterization of a Douglas fir forest, *Agricultural and Forest*
1195 *Meteorology*, 162–163, 115-126, 2012.

1196 Wharton, S., Schroeder, M., Paw U, K. T., Falk, M., and Bible, K.: Turbulence considerations for
1197 comparing ecosystem exchange over old-growth and clear-cut stands for limited fetch and
1198 complex canopy flow conditions, *Agricultural and Forest Meteorology*, 149, 1477-1490, 2009.

1199 Wohl, E., Barros, A., Brunzell, N., Chappell, N. A., Coe, M., Giambelluca, T., Goldsmith, S., Harmon, R.,
1200 Hendrickx, J. M. H., Juvik, J., McDonnell, J., and Ogden, F.: The hydrology of the humid tropics,
1201 *Nature Clim. Change*, 2, 655-662, 2012.

1202 Yan, Y., Zhao, B., Chen, J., Guo, H., Gu, Y., Wu, Q., and Li, B.: Closing the carbon budget of estuarine
1203 wetlands with tower - based measurements and MODIS time series, *Global Change Biology*, 14,
1204 1690-1702, 2008.

1205 Yao, Y., Liang, S., Li, X., Hong, Y., Fisher, J. B., Zhang, N., Chen, J., Cheng, J., Zhao, S., and Zhang, X.:
1206 Bayesian multimodel estimation of global terrestrial latent heat flux from eddy covariance,
1207 meteorological, and satellite observations, *Journal of Geophysical Research: Atmospheres*, 119,
1208 4521-4545, 2014.

1209 Zhu, Z., Bi, J., Pan, Y., Ganguly, S., Anav, A., Xu, L., Samanta, A., Piao, S., Nemani, R. R., and Myneni, R. B.:
1210 Global data sets of vegetation leaf area index (LAI) 3g and Fraction of Photosynthetically Active
1211 Radiation (FPAR) 3g derived from Global Inventory Modeling and Mapping Studies (GIMMS)
1212 Normalized Difference Vegetation Index (NDVI3g) for the period 1981 to 2011, *Remote Sensing*, 5,
1213 927-948, 2013.

1214 Zierl, B., Bugmann, H., and Tague, C. L.: Water and carbon fluxes of European ecosystems: An evaluation
1215 of the ecohydrological model RHESSys, *Hydrological processes*, 21, 3328-3339, 2007.

1216

1217 Table 1: Summary of data sources for tower-based and grid-based analysis and their spatial and
 1218 temporal resolutions.

Variable	Tower-based	Grid-based	Model
Air temperature	Tower data aggregated to 3-hourly	LandFlux data at 0.5° and 3-hourly	All models
Humidity	Tower-based relative humidity converted to specific humidity and aggregated to 3-hourly	Specific humidity from LandFlux data at 0.5° and 3-hourly	All except GLEAM
Pressure	Calculated as a function of ground elevation	LandFlux data at 0.5° and 3-hourly	All models
Net radiation	Tower data aggregated to 3-hourly	LandFlux data from SRB v3 at 1° and 3-hourly	All models
Ground heat flux	Tower data aggregated to 3-hourly	Calculated from net radiation and fractional vegetation cover data, 0.5° and 3-hourly	All models
Land surface temperature	Calculated from tower-based longwave upward radiation and aggregated to 3-hourly	LandFlux data at 0.5° and 3-hourly	SEBS only
Wind speed	Tower data aggregated to 3-hourly	LandFlux data at 0.5° and 3-hourly	SEBS only
Canopy height	Tower meta data	JPL product and Equation 1	SEBS only
NDVI	GIMMS NDVI at 8km and bi-monthly	GIMMS NDVI at 0.5° and bi-monthly	All except GLEAM
Leaf area index	Calculated from NDVI	LandFlux data at 0.5° and monthly	SEBS and PM-Mu
Fractional vegetation cover	Not used as ground heat flux is available.	Calculated from NDVI	All except GLEAM
Precipitation	Tower data aggregated to 3-hourly	LandFlux data at 0.5° and 3-hourly	GLEAM only
Soil properties	IGBP-DIS at 5 arc-minutes	IGBP-DIS data aggregated to 0.5°	GLEAM only
Soil moisture	CCI-WACMOS data at 0.25° and daily	Same as tower-based	GLEAM only
Soil depth	GlobSnow (daily and 25 km)	Same as tower-based	GLEAM only
Vegetation optical depth	From Liu et al. (2011b) at 0.25° and daily	Same as tower-based	GLEAM only
Snow water equivalent	GlobSnow and NSIDC at 0.25° and daily	Same as tower-based	GLEAM only
Lightning frequency	Monthly climatology at 0.5°	Same as tower-based	GLEAM only
Cover fractions	MOD44B data at 250 m	MOD44B data at 0.5°	GLEAM only

1220 Figure 1: Location of the selected towers and their distributions for various biomes

1221 Figure 2: Scatterplots of observed versus simulated latent heat flux for tower-based data.
1222 Colors show the frequency of values from high (red) to low (yellow). The thick black line
1223 represents the linear regression, while the thin line is the 1:1 line. The series of small circles
1224 show the percentile increments of data from the 1st to 99th, with large circles denoting the 25th,
1225 50th and 75th percentiles. The statistics shown on each figure provide coefficient of
1226 determination (R^2), slope (m), y-intercept (b), number of data records (n), the root-mean-
1227 squared difference (RMSD), relative error (RE) and the Nash-Sutcliffe Efficiency (NSE).

1228 Figure 3: Scatterplots of observed versus simulated evaporation for grid-based data. Colors
1229 show the frequency of values from high (red) to low (yellow). The thick black line is the linear
1230 regression and the thin line is the 1:1 line. The series of small circles show the percentile
1231 increments of data from the 1st to 99th, with large circles denoting the 25th, 50th and 75th
1232 percentiles. The statistics shown on the graphs are coefficient of determination (R^2), slope (m),
1233 y-intercept (b), number of data records (n), the root-mean-squared difference (RMSD), relative
1234 error (RE) and the Nash-Sutcliffe Efficiency (NSE).

1235 Figure 4: Comparison of the performance skill of the models in reproducing evaporation for the
1236 tower-based analyses. R^2 is the coefficient of determination, RE is relative error (lower is better)
1237 and NSE is the Nash-Sutcliffe Efficiency (higher is better). Towers are arranged from left to right
1238 based on an aridity index (secondary y-axis).

1239 Figure 5: Coefficient of determination (R^2), relative error (RE) and Nash-Sutcliffe Efficiency (NSE)
1240 for models across different biome types. Each point represents the collection of all available 3-
1241 hourly records of towers located within the selected biome, with the number of towers shown
1242 on the secondary y-axis of the R^2 plot in red. NSE for the shrubland response of SEBS is printed.

1243

1244 Figure 6: Percentile plots of observed (x-axis) versus estimated latent heat flux (y-axis) at 3-
1245 hourly resolution for the tower-based analysis across the seven studied biomes. Percentiles
1246 encompass the 1st to 99th range in 1 percent increments, with Q_{25} , Q_{50} and Q_{75} denoted by large
1247 coloured circles.

1248 Figure 7: The upper panel presents Nash-Sutcliffe Efficiency (NSE; x-axis) and R^2 (color tone)
1249 between tower- and grid-based values for net radiation, land surface temperature, air
1250 temperature, wind speed, specific humidity, fractional vegetation cover and leaf area index,
1251 across the seven studied biome types. The lower panel presents the NSE (x-axis) and R^2 of
1252 model simulated evaporation against closure-corrected observed values. The number of towers
1253 for each biome type used in the analysis are shown in red font on the secondary (right) axis in
1254 each of the plots. Statistics for those results beyond the range of the x-axis are printed
1255 separately on the plot.

1256 Figure 8: Coefficient of determination (R^2), relative error (RE) and Nash-Sutcliffe Efficiency (NSE)
1257 for model simulated results across the five different climate zones (y-axis). The zones are
1258 represented by dryland (DRY), temperate continental (TempCONT), temperate (TEMP), sub-
1259 tropical (subTRO) and boreal (BOR). Each point represents the collection of all towers located
1260 within the selected climate zone, with the number of towers shown on the secondary y-axis of
1261 the R^2 panel in red.

1262 Figure 9: Percentile plots of observed (x-axis) versus estimated latent heat flux (y-axis) at 3-
1263 hourly resolution for tower-based analysis and across the different climate zones. Percentiles
1264 encompass the 1st to 99th range in 1 percent increments. Q_{25} , Q_{50} and Q_{75} are denoted by large
1265 circles.

1266

1267

1268 Figure 10: The upper panel shows Nash-Sutcliffe Efficiency (NSE; x-axis) and R^2 (color tone)
1269 between tower-based and grid-based values for net radiation, land surface temperature, air
1270 temperature, wind speed, specific humidity, fractional vegetation cover and leaf area index
1271 across the five different climate zones. The lower panel shows NSE (x-axis) and R^2 of model
1272 simulated evaporation against closure-corrected observed values across climate zones. The
1273 number of towers for each biome are shown in red font on the secondary (right) axis of the
1274 plots. Statistics for the grid-based SEBS result over dry climate zone are printed.

1275

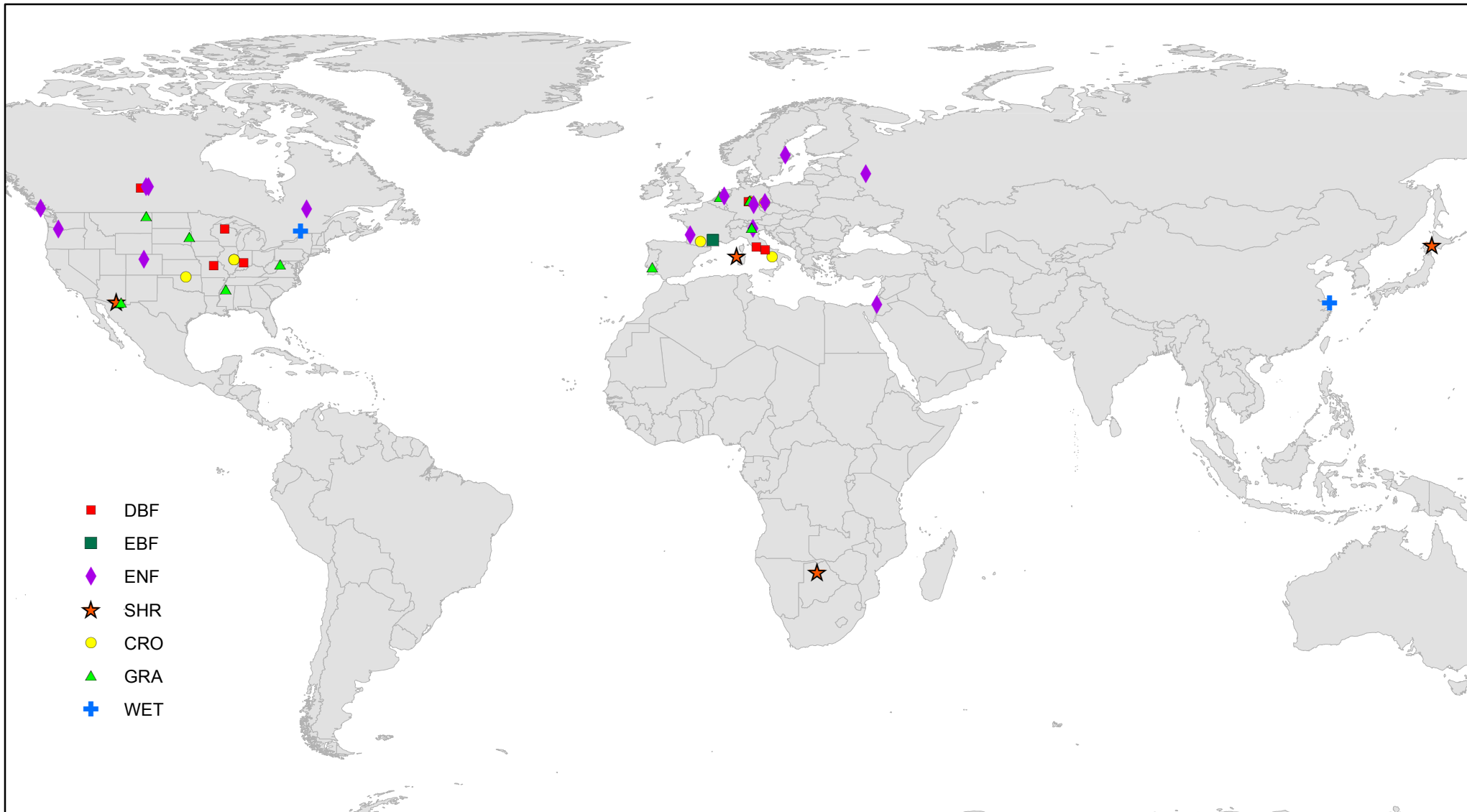


Figure 1

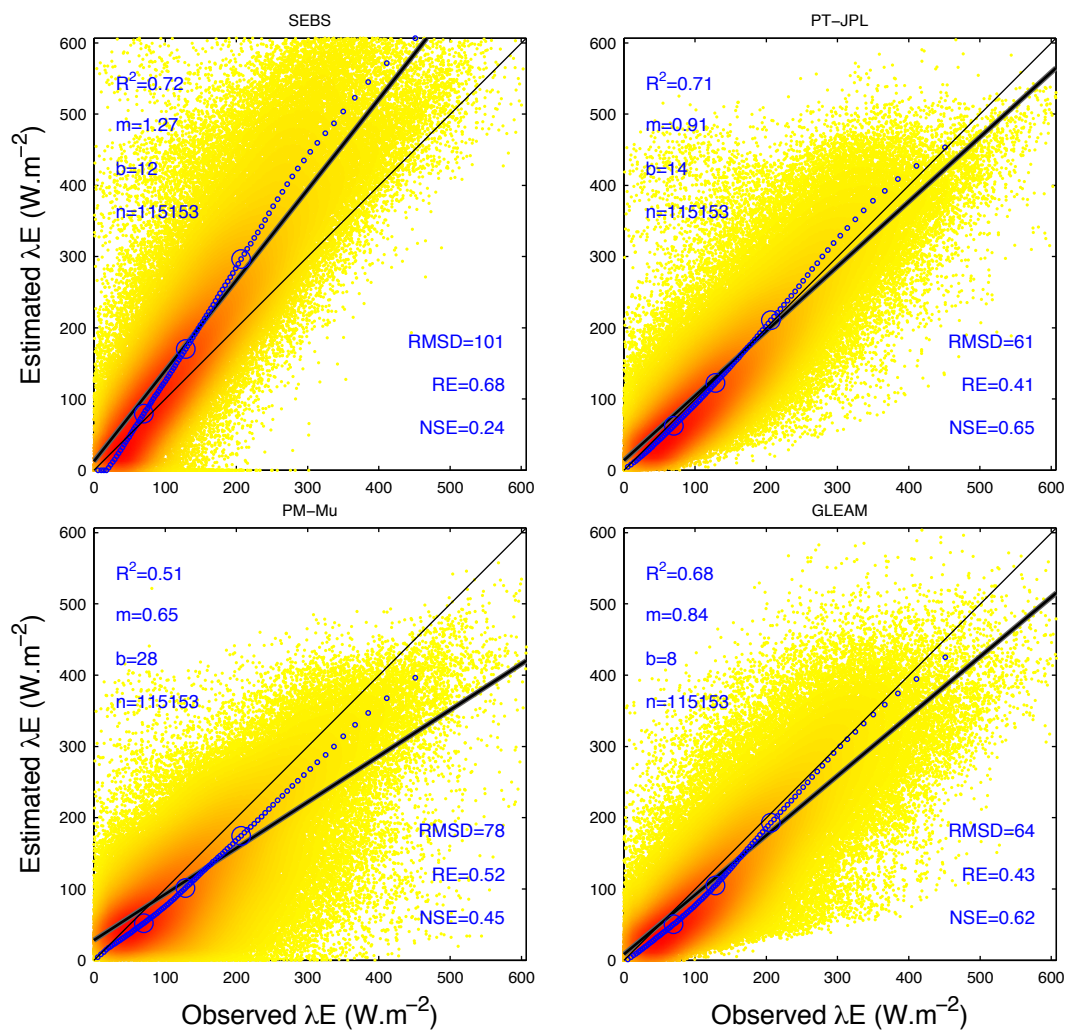


Figure 2

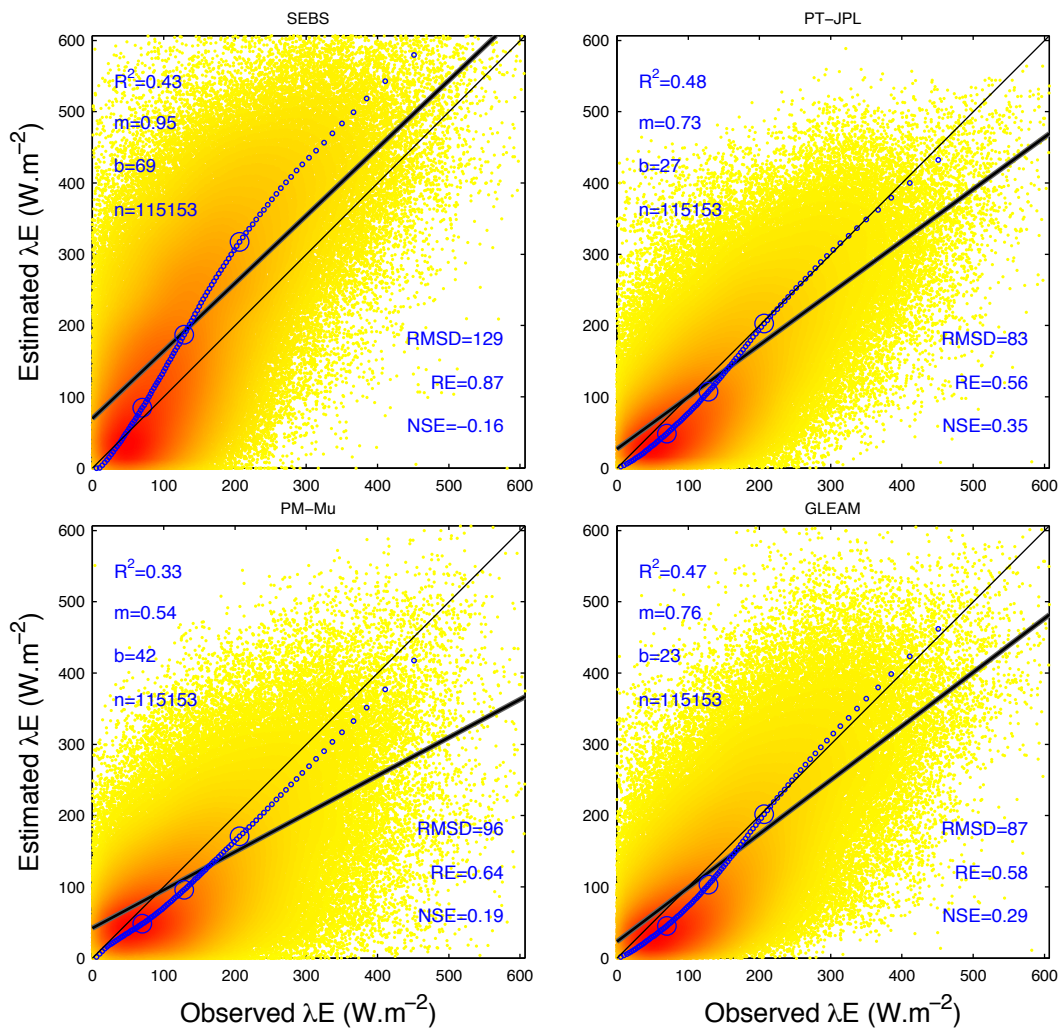


Figure 3

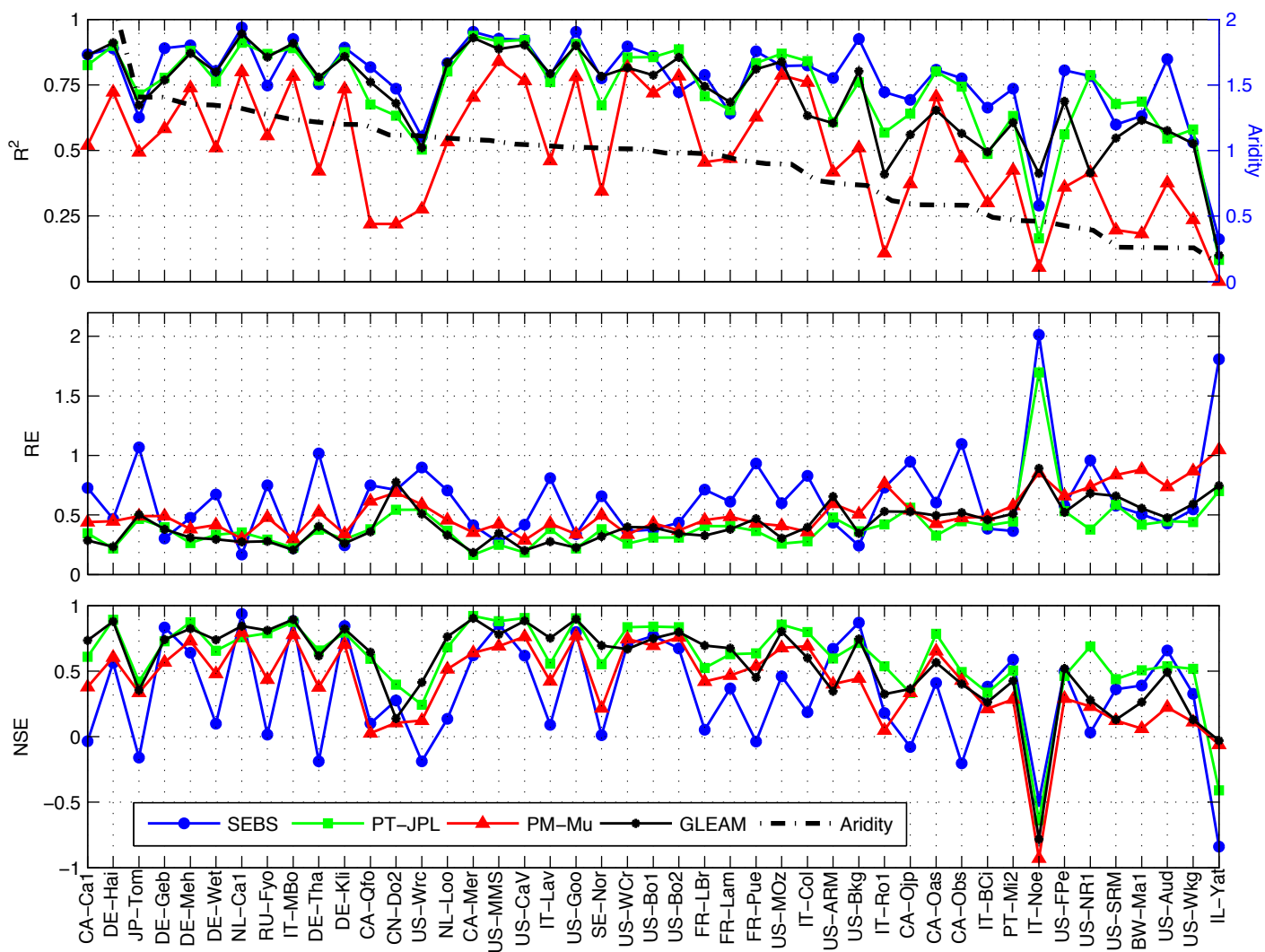


Figure 4

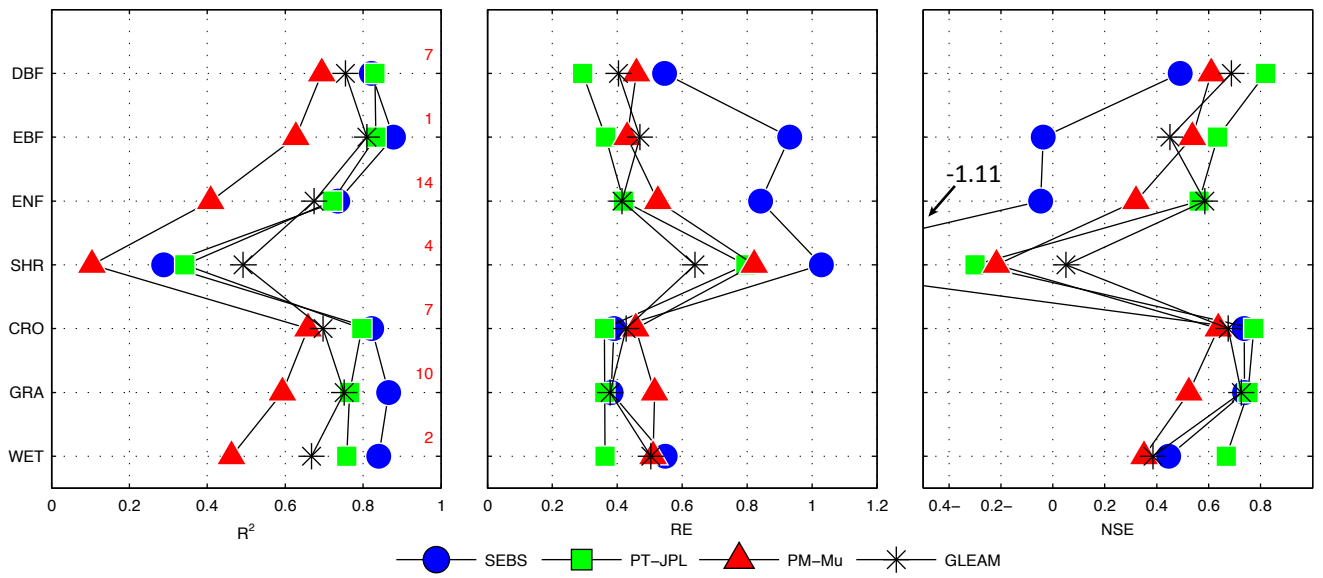


Figure 5

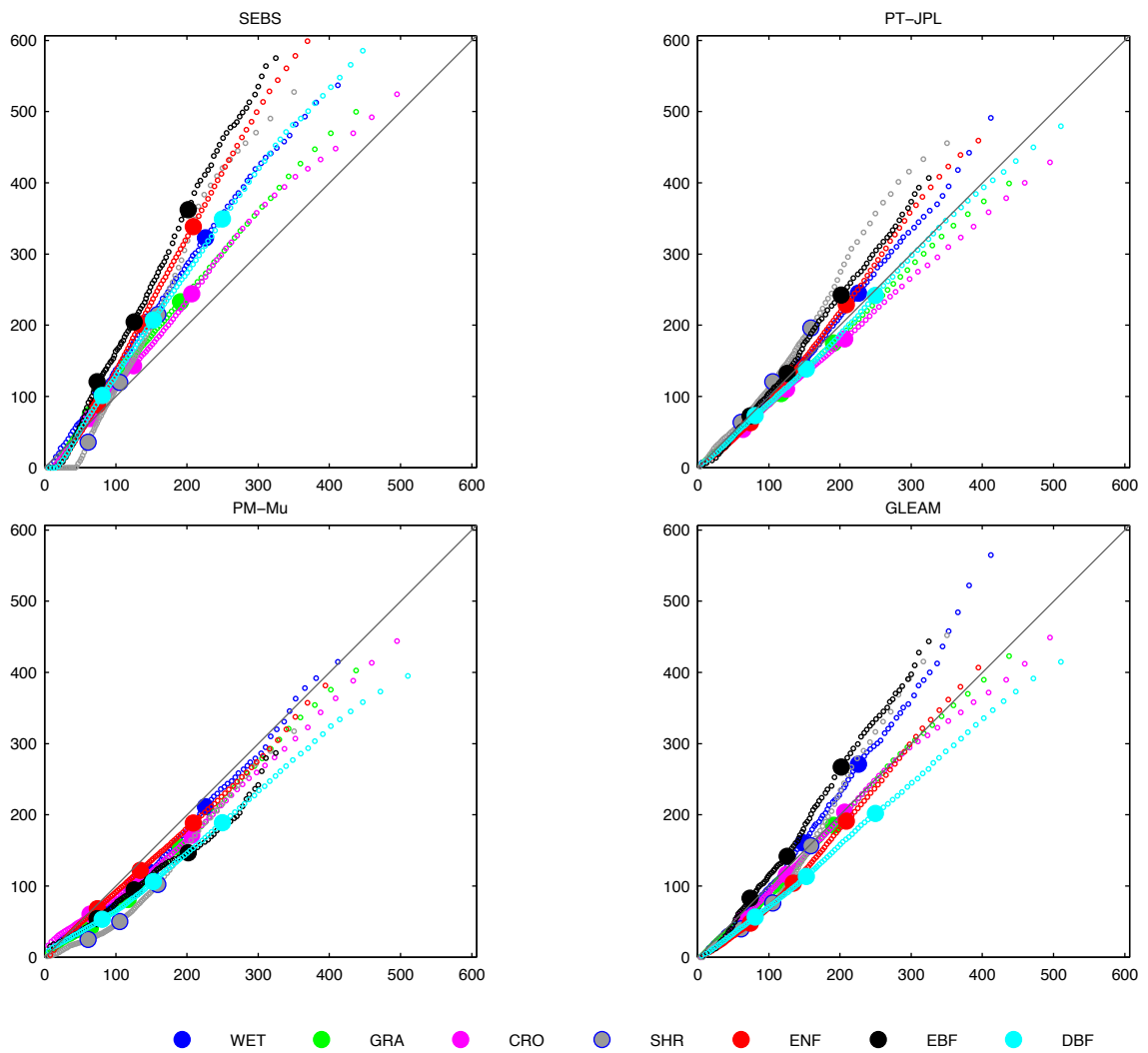


Figure 6

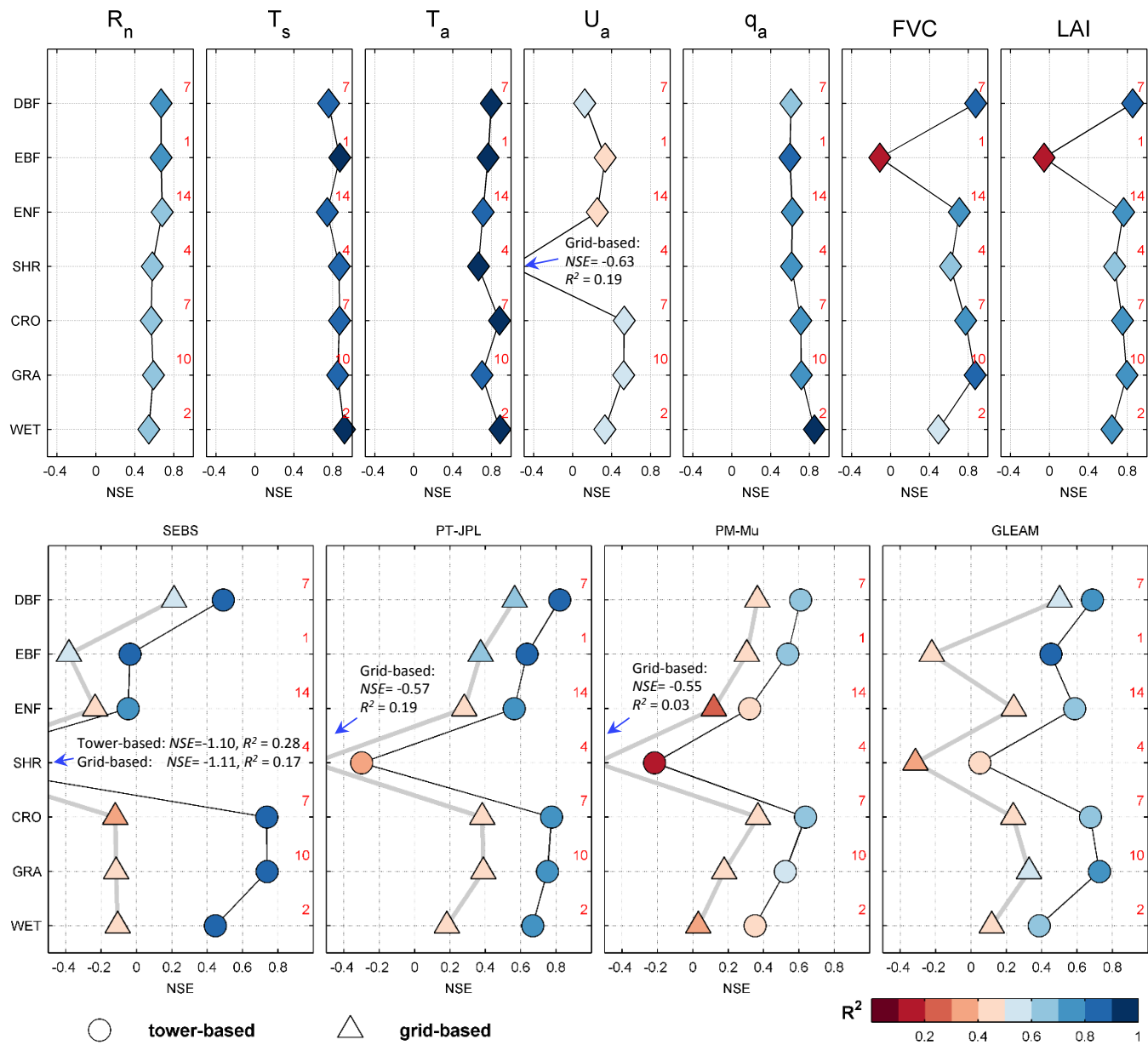


Figure 7

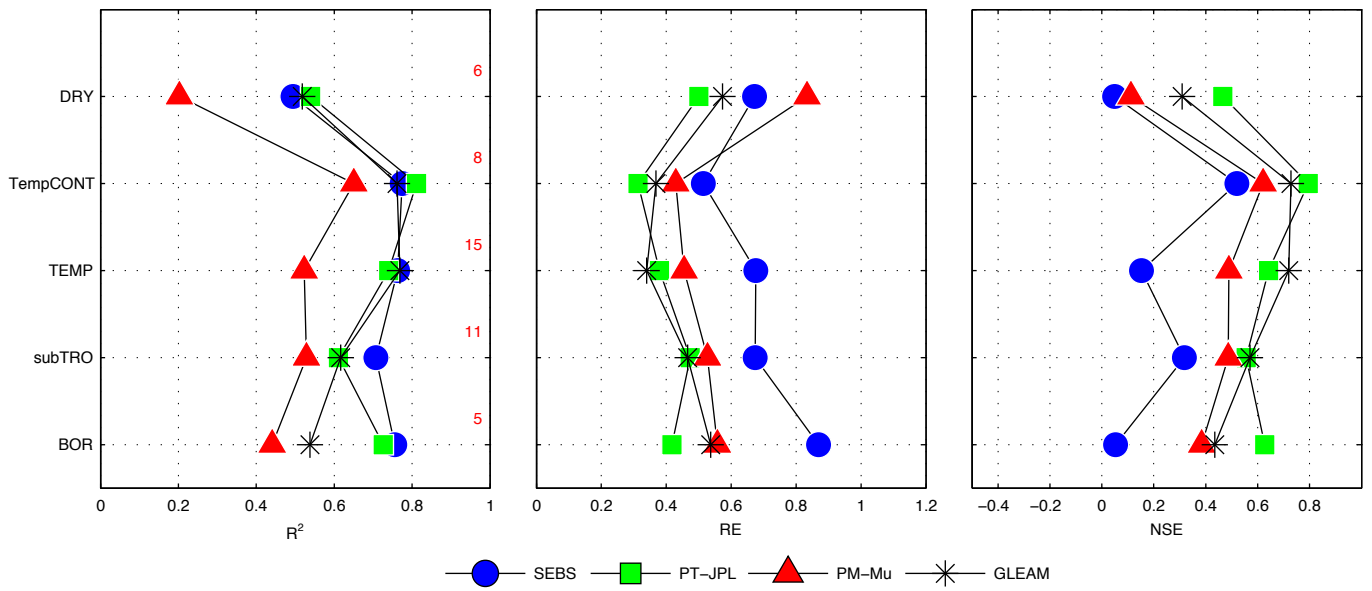


Figure 8

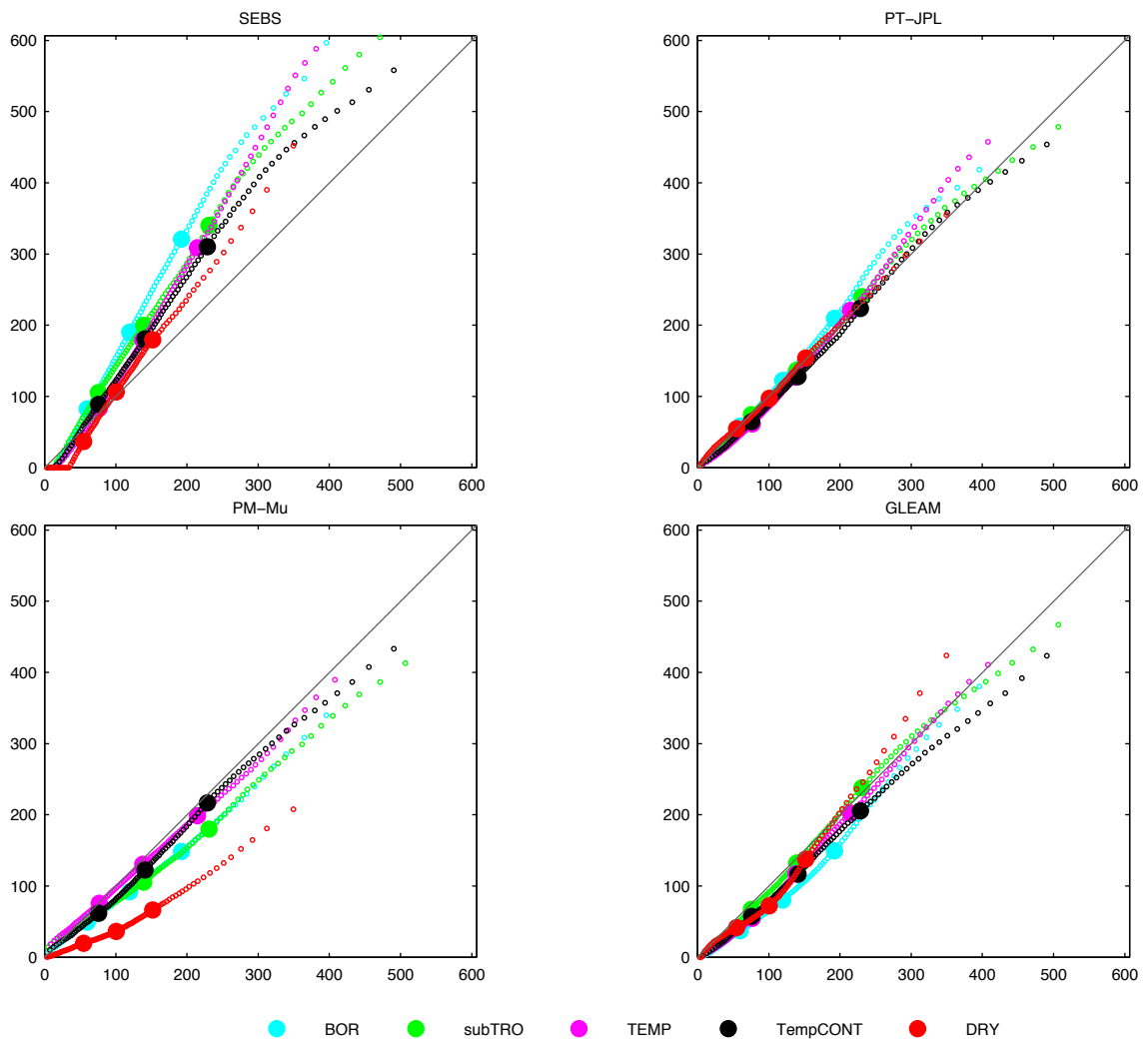


Figure 9

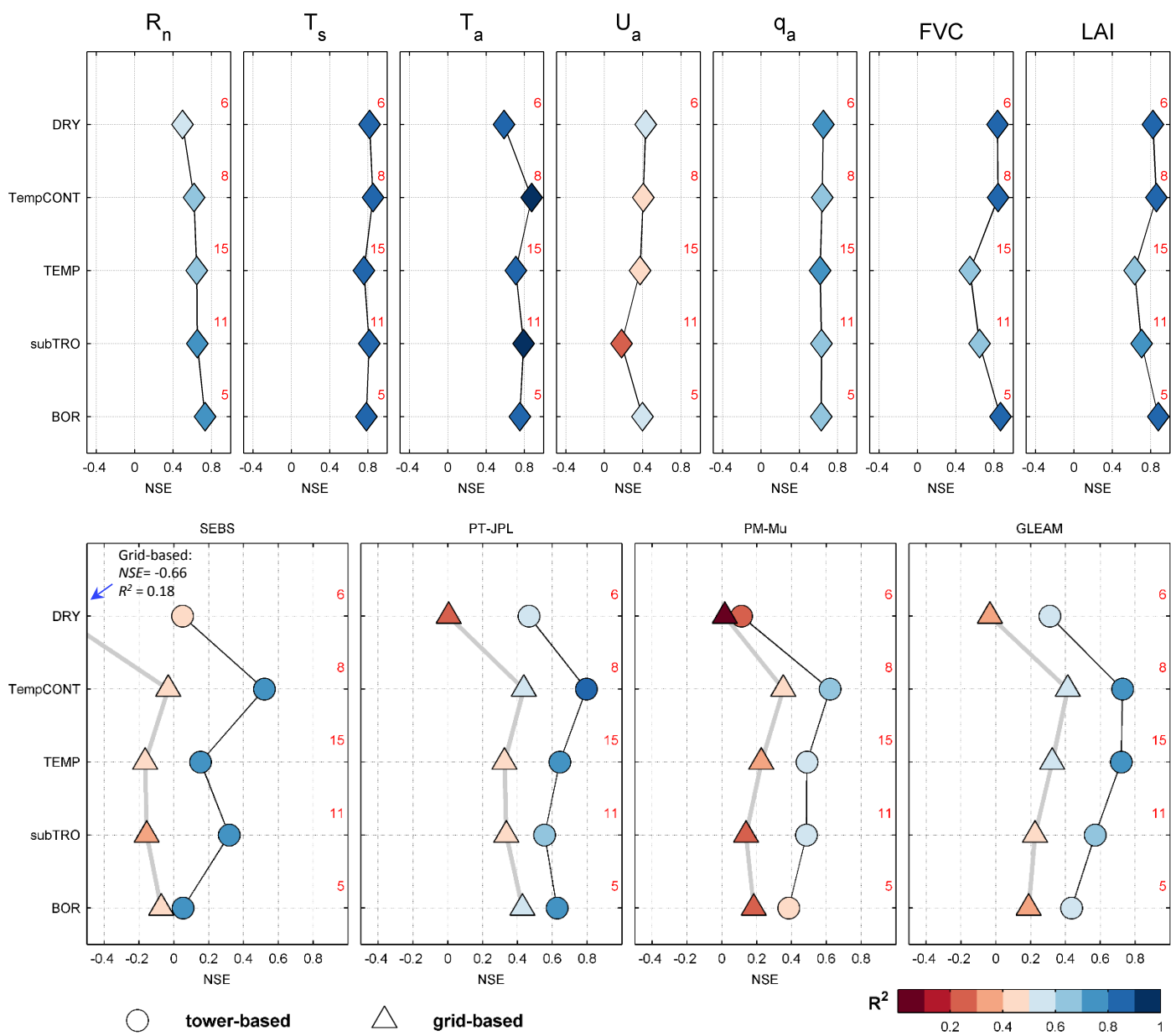


Figure 10